Inorganic Chemistry
Article

Inorg. Chem. **2009**, *48*, 7211–7229 **7211**
DOI: 10.1021/ic9006197

One-Step and Two-Step Spin-Crossover Iron(II) Complexes of ((2-Methylimidazol-4-yl)methylidene)histamine

Tetsuya Sato,[†] Koshiro Nishi,[†] Seiichiro Iijima,[‡] Masaaki Kojima,[§] and Naohide Matsumoto*[,†]

[†]*Department of Chemistry, Faculty of Science, Kumamoto University, Kurokami 2-39-1, Kumamoto 860-8555, Japan,* [‡]*National Institute of Advanced Industrial Science and Technology, Tsukuba 305-8566, Japan, and* [§]*Department of Chemistry, Faculty of Science, Tsushima-naka 3-1-1, Okayama 700-8530, Japan*

Received March 31, 2009

A tridentate ligand ((2-methylimidazol-4-yl)methylidene)histamine (abbreviated as $H_2L^{2\text{-Me}}$), that is, the 1:1 condensation product of 2-methyl-4-formylimidazole and histamine, was used for the syntheses of a new family of iron(II) spin-crossover (SCO) complexes with the general chemical formulas $[Fe(H_2L^{2\text{-Me}})_2]X_2\cdot$solvent (X = Cl, ClO_4, and BPh_4; solvent = 2-PrOH and CH_3CN) and $[Fe(H_2L^{2\text{-Me}})_2]X\cdot Y\cdot$solvent (X = Cl and Br; Y = ClO_4, BF_4, PF_6, and AsF_6; solvent = EtOH and 2-PrOH). The complex cation $[Fe(H_2L^{2\text{-Me}})_2]^{2+}$ is a chiral species due to an octahedral coordination of two unsymmetrical tridentate ligands, has a ligand field strength around the spin-crossover point, and is hydrogen-bonded to anions to form a variety of network structures. The dichloride complexes $[Fe(H_2L^{2\text{-Me}})_2]Cl_2\cdot$2-PrOH$\cdot 0.5H_2O$ (**1**) and $[Fe(H_2L^{2\text{-Me}})_2]Cl_2\cdot$2-PrOH$\cdot H_2O$ (**1′**) have a one-dimensional (1D) structure, in which adjacent two chiral complex-cations are doubly bridged by two Cl^- ions through NH(histamine)$\cdots Cl^-\cdots$HN(2-methyl-4-formylimidazole) hydrogen bonds to give a chiral 1D rod. The chiral rods with the same chirality are stacked in the crystal lattices to give a conglomerate, **1**, and those with the opposite chiralities are stacked to give a racemic compound, **1′**. The enantiomeric circular dichromism spectra of **1** gave definitive evidence of the conglomerate. Compound **1** showed a two-step SCO, while the desolvated sample showed a steep one-step SCO at $T_{1/2}$ = 180 K. A series of complexes, $[Fe(H_2L^{2\text{-Me}})_2]Cl\cdot X\cdot$EtOH (X = ClO_4 (**2a**), BF_4 (**2b**), PF_6 (**2c**), and AsF_6 (**2d**)), $[Fe(H_2L^{2\text{-Me}})_2]Cl\cdot ClO_4\cdot 0.5$(1-PrOH)$\cdot 1.5H_2O$ (**2a′**), and $[Fe(H_2L^{2\text{-Me}})_2]Br\cdot ClO_4\cdot 0.5$EtOH (**2a″**), display an isomorphous two-dimensional (2D) network at room temperature (296 K), in which the structure is constructed by the NH$\cdots Cl^-$ (or Br^-) hydrogen bonds between the imidazole NH groups of $[Fe(H_2L^{2\text{-Me}})_2]^{2+}$ and the Cl^- (or Br^-) ion as a connector. The complexes showed a variety of SCO properties depending on the anion, solvent molecule, and the kind of bridging halogen ion. The complexes of ClO_4^- (**2a**, **2a′**, **2a″**) and BF_4^- (**2b**) with smaller anions showed a two-step SCO with a wide temperature region of the intermediate state of (high-spin (HS) + low-spin (LS))/2 state, their values of ($T_{1/2,1}$, $T_{1/2,2}$) being (75, 255 K), (100, 220 K), (110, 220 K), and (100, 260 K), respectively, where the crystal changes from monoclinic $P2_1/n$ in the HS state to triclinic $P\bar{1}$ in the intermediate state. The complexes of PF_6^- (**2c**) and AsF_6^- (**2d**) with larger anions showed a one-step SCO at $T_{1/2}$ = 198 and 173 K, respectively, in which the crystal system and space group showed no change during the spin transition. The crystal solvent and halide ion also affected the completeness of the SCO in the lower-temperature region and the steepness of the SCO profile. The experimental results were correlated to the theoretical results based on an Ising-like model. $[Fe(H_2L^{2\text{-Me}})_2](BPh_4)_2\cdot CH_3CN$ (**3**) has no network structure. $[Fe(H_2L^{2\text{-Me}})_2](ClO_4)_2$ (**4**) assumes a chiral 3D network structure constructed by the hydrogen bonds between the imidazole groups of one enantiomorph $[Fe(H_2L^{2\text{-Me}})_2]^{2+}$ and the bridging ClO_4^- ion. Compounds **3** and **4** in the solid states are in the HS state, demonstrating that the formation of imidazole$-Cl^-$ or Br$-$hydrogen bonds can give SCO properties, but the hydrogen bond of imidazole$-ClO_4^-$ cannot give SCO.

Introduction

Spin-crossover (SCO) is a representative example of molecular bistability, in which the high-spin (HS) and low-spin (LS) states are interconvertible by physical perturbations such as temperature, pressure, or light.[1] Since the first discovery of the SCO phenomenon in tris(dithiocarbamato)-iron(III), the phenomenon of SCO has attracted much attention from chemists, biochemists, and physicists,[1a] because it offers an understanding of ligand field theory and the functions of certain haem systems; moreover, it has potential applications in switching and sensing devices.[2] In addition to

*To whom correspondence should be addressed. E-mail: naohide@aster.sci.kumamoto-u.ac.jp.

(1) (a) Gütlich, P.; Goodwin, H. A. *Top. Curr. Chem.* **2004**, 233−235; Spin Crossover in Transition Metal Compounds I−III. (b) Gütlich, P.; Garcia, Y.; Goodwin, H. A. *Chem. Soc. Rev.* **2000**, *29*, 419–427. (c) Gütlich, P.; Hauser, A.; Spiering, H. *Angew. Chem., Int. Ed. Engl.* **1994**, *33*, 2024. (d) Goodwin, H. A. *Coord. Chem. Rev.* **1976**, *18*, 293–325. (e) Gütlich, P. *Struct. Bonding (Berlin)* **1981**, *44*, 83. (f) König, E.; Ritter, G.; Kulshreshtha, S. K. *Chem. Rev.* **1985**, *85*, 219. (g) König, E. *Struct. Bonding (Berlin)* **1991**, *76*, 51. (h) Real, J. A.; Gaspar, A. B.; Niel, V.; Muñoz, M. C. *Coord. Chem. Rev.* **2003**, *235*, 121.

(2) (a) Kahn, O.; Martinez, C. J. *Science* **1998**, *279*, 44. (b) van Koningsbruggen, P. J.; Garcia, Y.; Kahn, O.; Fournes, L.; Kooijman, H.; Spek, A. L.; Haasnoot, J. G.; Moscovici, J.; Provost, K.; Michalowicz, A.; Renz, F.; Gütlich, P. *Inorg. Chem.* **2000**, *39*, 1891–1900. (c) Real, J. A.; Andres, E.; Munoz, M. C.; Julve, M.; Granier, T.; Bousseksou, A.; Varret, F. *Science* **1995**, *268*, 265–267. (d) Hayami, S.; Danjobara, K.; Inoue, K.; Ogawa, Y.; Matsumoto, N.; Maeda, Y. *Adv. Mater.* **2004**, *16*, 869. (e) Kahn, O.; Launay, J. P. *Chemtronics* **1988**, *3*, 140.

Published on Web 07/02/2009

temperature as an external perturbation, spin-state transition induced by other physical inputs such as pressure, magnetic field, light, ultrashort laser pulse, soft- and hard-X-ray radiations, and nuclear decay have been discovered.[3] It is expected that SCO can be used in multisensing devices. While SCO is essentially described as a phenomenon of a single molecule, interesting SCO behaviors observed in the solid state, such as abrupt and multistep SCO and hysteresis, have been ascribed to a cooperative effect between the SCO sites.[1] Coordination chemists have gone through a lot of effort in the synthesis of SCO complexes exhibiting a cooperative effect. From the synthetic viewpoint, to achieve a cooperative effect, polymeric SCO complexes with bridging ligands[4] and mononuclear SCO complexes exhibiting intermolecular hydrogen bonding[5] or $\pi-\pi$ stacking[6] have been synthesized, and among them, interesting SCO behaviors have been discovered. When coordination chemists design and synthesize new SCO complexes, the most important property in their minds would be a wide thermal hysteresis around room temperature. Among the SCO complexes studied over 80 years, 1D tris-μ-triazole Fe^{II} complex $[Fe^{II}$(4-amino-1,2,4-triazole)$_3$](2-naphthalene sulfonate)$_2\cdot x$H$_2$O[4a] and 2D Fe^{III} complex, with $\pi-\pi$ stacking, $[Fe^{III}(pap)_2]ClO_4\cdot H_2O$[6a] (Hpap is a tridentate ligand formed by the 1:1 condensation of *o*-aminophenol and pyridine-2-carbaldehyde) can be two representative and successful examples with respect to wide thermal hysteresis around room temperature, where the SCO sites are connected by rather strong coordination bonds for the former complex and by weak $\pi-\pi$ interactions for the latter complex, respectively. The results demonstrate that strong interaction in bond strength is not always necessary, but "effective cooperativity" is needed to achieve valuable SCO properties such as hysteresis and steepness. From the theoretical side, Ising-like models have been used in order to take into account the cooperativity in the SCO transition,[7] and the origin of the cooperative nature has been investigated by considering elastic interactions among molecules.[8] As the size of each molecule changes depending on its spin state, the elastic interaction among the lattice distortions provides the cooperative interaction of the spin states. However, it means that the parameters of the theoretical model calculations are not straightforward to synthetic chemists in the molecular design of SCO complexes. In fact, SCO behaviors in the solid state are influenced by many factors in very complicated manners, and our synthetic chemists seem to have no reliable or rational guide to achieving the objective SCO. Therefore, the correlation between the theoretical predictions and the structural parameter must be established. In order to approach this problem, a series of SCO complexes having the same network structure while showing different SCO properties will be helpful to understanding the spin transition behavior from experimental and theoretical viewpoints.

We have reported on the metal complexes of polydentate ligands containing imidazole groups.[9] Iron complexes with polydentate ligands derived from the condensation reaction of 4-formylimidazole derivatives and various polyamines have been found to be a new family of SCO complexes.[10] These iron complexes assume various types of 1D and 2D extended network structures constructed by the various types of hydrogen bonds such as imidazole−imidazolato hydrogen bonds (NH···N), NH···Cl^-, and NH···π, and they showed a variety of SCO behaviors, such as gradual, steep, and multistep SCO.

In this work, we have focused on a tridentate ligand with unsymmetrical N_3 donor atoms derived from the 1:1 condensation reaction of 2-methyl-4-formylimidazole and histamine, $H_2L^{2\text{-Me}}$ = ((2-methylimidazol-4-yl)methylidene)histamine, which involves two imidazole groups per ligand. The ligand reacts with an Fe^{II} ion in a 2:1 molar ratio to produce a chiral complex $[Fe(H_2L^{2\text{-Me}})_2]^{2+}$ (Chart 1). This complex has octahedral coordination geometry with N_6 donor atoms, and the four imidazole (NH) sites per complex can function to form a hydrogen bond network. By using the complex cation

(3) (a) Decurtins, S.; Gütlich, P.; C. P.; Köhler; Spiering, H.; Hauser, A. *Chem. Phys. Lett*. **1984**, *105*, 1–4. (b) Vanko, G.; Renz, F.; Molnar, G.; Neisius, T.; Karpati, S. *Angew. Chem., Int. Ed*. **2007**, *46*, 5306. (c) Gütlich, P.; Hauser, A.; Spiering, H. *Angew. Chem., Int. Ed. Engl*. **1994**, *33*, 2024–2054. (d) Gütlich, P.; van Koningsbruggen, P. J.; Renz, F. *Struct. Bonding (Berlin)* **2004**, *107*, 27–75. (e) Qui, Y.; Muller, E. W.; Spiering, H.; Gütlich, P. *Chem. Phys. Lett*. **1983**, *101*, 503. (f) Garcia, Y.; Kahn, O.; Ader, J. P.; Buzdin, A.; Meudesoif, Y.; Guillot, M. *Phys. Lett*. **2000**, *A 271*, 145. (g) Jeftic, J.; Hauser, A. *J. Phys. Chem*. **1997**, *B 101*, 10 262. (h) Niel, V.; Muñoz, M. C.; Gaspar, A. B.; Galet; Levchenko, G.; Real, J. A. *Chem.—Eur. J*. **2002**, *8*, 2446. (i) Bousseksou, A.; Negre, N.; Goiran, M.; Salmon, I.; Tuchagues, J.-P.; Boillot, M. L.; Boukhddaden, K.; Varret, F. *Eur. Phys. J*. **2000**, *B13*, 451.

(4) (a) Kröber, J.; Codjovi, E.; Kahn, O.; Grolière, F.; Jay, C. *J. Am. Chem. Soc*. **1993**, *115*, 9810. (b) Real, J. A.; Gaspar, A. B.; Niel, V.; Muñoz, M. C. *Coord. Chem. Rev*. **2003**, *235*, 121. (c) Galet, A.; Muñoz, M. C.; Gaspar, A. B.; Real, J. A. *Inorg. Chem*. **2005**, *44*, 8749. (d) van Koningsbruggen, P. J.; Garcia, Y.; Codjovi, E.; Lapouyade, R.; Kahn, O.; Fournes, L.; Rabardel, L. *J. Mater. Chem*. **1997**, *7*, 2069. (f) Imatomi, S.; Sato, T.; Hashimoto, S.; Matsumoto *Eur. J. Inorg. Chem*. **2009**, 721–726.

(5) (a) Buchen, T.; Gütlich, P.; Sugiyarto, K. H.; Goodwin, H. A. *Chem.—Eur. J*. **1996**, *2*, 1134–1138. (b) Sugiyarto, K. H.; Scudder, M. L.; Craig, D. C.; Goodwin, H. A. *Aust. J. Chem*. **2000**, *53*, 755–765. (c) Sugiyarto, K. H.; Goodwin, H. A. *Aust. J. Chem*. **1988**, *41*, 1645–1663. (d) Sunatsuki, Y.; Ikuta, Y.; Matsumoto, N.; Ohta, H.; Kojima, M.; Iijima, S.; Hayami, S.; Maeda, Y.; Kaizaki, S.; Dahan, F.; Tuchagues, J.-P. *Angew. Chem., Int. Ed*. **2003**, *42*, 1614–1618.

(6) (a) Hayami, S.; Gu, Z.; Shiro, M.; Einaga, Y.; Fujishima, A.; Sato, O. *J. Am. Chem. Soc*. **2000**, *122*, 7126. (b) Hayami, S.; Gu, Z.; Yoshiki, H.; Fujishima, A.; Sato, O. *J. Am. Chem. Soc*. **2001**, *123*, 11644.

(7) (a) Wajnflasz, J.; Pick, R. *J. Phys. (Paris)* **1971**, *Colloq. 32*, C1–91. (b) Bosseksou, A.; Varret, F.; Nasser, J. J. *Phys*. **1993**, *I3*, 1463. (c) Nishino, M.; Bouheddaden, K.; Miyashita, S.; Varret, F. *Phys. Rev*. **2003**, *B 68*, 224402.

(8) (a) Nishino, M.; Bouheddaden, K.; Konishi, Y.; Miyashita, S. *Phys. Rev. Lett*. **2007**, *98*, 247203. (b) Konishi, Y.; Tokoro, H.; Nishino, M.; Miyashita, S. *Phys. Rev. Lett*. **2008**, *100*, 067206. (c) Miyashita, S.; Konishi, Y.; Nishino, M.; Tokoro, H.; Rikvold, P. A. *Phys. Rev. B 77*, **2008**, 014105. (d) Spiering, H. *Top. Curr. Chem*. **2004**, *235*, 171−195.

(9) (a) Sunatsuki, Y.; Motoda, Y.; Matsumoto, N. *Coord. Chem. Rev*. **2002**, *226*, 199–209. (b) Shii, Y.; Matsuo, T.; Kai, F.; Nakashima, T.; Tuchagues, J. P.; Matsumoto, N. *Inorg. Chem*. **1999**, *38*, 3513–3522. (c) Katsuki, I.; Sunatsuki, Y.; Matsumoto, N.; Nakashima, T.; Kojima, M. *J. Am. Chem. Soc*. **2002**, *124*, 629–640. (d) Matsumoto, N.; Motoda, Y.; Matsuo, T.; Nakashima, T.; Re, N.; Dahan, F.; Tuchagues, J. P. *Inorg. Chem*. **1999**, *38*, 1165–1173.

(10) (a) Yamada, M.; Hagiwara, H.; Torigoe, H.; Matsumoto, N.; Kojima, M.; Dahan, F.; Tuchagues, J.-P.; Re, N.; Iijima, S. *Chem.—Eur. J*. **2006**, *12*, 4536–4549. (b) Ikuta, Y.; Ooidemizu, M.; Yamahata, Y.; Yamada, M.; Osa, S.; Matsumoto, N.; Iijima, S.; Sunatsuki, Y.; Kojima, M.; Dahan, F.; Tuchagues, J.-P. *Inorg. Chem*. **2003**, *42*, 7001–7017. (c) Yamada, M.; Ooidemizu, M.; Ikuta, Y.; Osa, S.; Matsumoto, N.; Iijima, S.; Kojima, M.; Dahan, F.; Tuchagues, J.-P. *Inorg. Chem*. **2003**, *42*, 8406–8416. (d) Sunatsuki, Y.; Ohta, H.; Kojima, M.; Ikuta, Y.; Goto, Y.; Matsumoto, N.; Iijima, S.; Akashi, H.; Kaizaki, S.; Dahan, F.; Tuchagues, J.-P. *Inorg. Chem*. **2004**, *43*, 4154–4171. (e) Yamada, M.; Fukumoto, E.; Ooidemizu, M.; Bréfuel, N.; Matsumoto, N.; Iijima, S.; Kojima, M.; Re, N.; Dahan, F.; Tuchagues, J.-P. *Inorg. Chem*. **2005**, *44*, 6967–6974. (f) Bréfuel, N.; Imatomi, S.; Torigoe, H.; Hagiwara, H.; Shova, S.; Meunier, J. -F.; Bonhommeau, S.; Tuchagues, J. -P.; Matsumoto, N. *Inorg. Chem*. **2006**, *45*, 8126–8135. (g) Arata, S.; Torigoe, H.; Iihoshi, T.; Matsumoto, N.; Dahan, F.; Tuchagues, J.-P. *Inorg. Chem*. **2005**, *44*, 9288–9292. (h) Hagiwara, H.; Hashimoto, S.; Matsumoto, N.; Iijima, S. *Inorg. Chem*. **2007**, *46*, 3136–3143. (i) Arata, S.; Hamamatsu, T.; Sato, T.; Iihoshi, T.; Matsumoto, N.; Iijima, S. *Chem. Lett*. **2007**, 778–779.

Chart 1. Schematic Drawings of $[Fe(H_2L^{2\text{-}Me})_2]^{2+}$ and Two Enantiomorphs

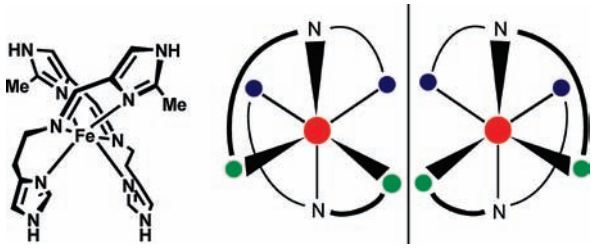

$[Fe(H_2L^{2\text{-}Me})_2]^{2+}$, various anions, and various crystal solvents, we can synthesize the complexes with general chemical formulas of $[Fe(H_2L^{2\text{-}Me})_2]X_2\cdot$solvent (X = Cl, BPh_4, ClO_4) and $[Fe(H_2L^{2\text{-}Me})_2]X\cdot Y\cdot$solvent (X = Cl, Br; Y = ClO_4, BF_4, PF_6, AsF_6). These complexes have versatile networks constructed by hydrogen bonds involving 1D, 2D, and 3D network structures as well as non-network structures. The complexes $[Fe(H_2L^{2\text{-}Me})_2]Cl_2\cdot$solvent (**1** and **1′**) have a chiral 1D rodlike structure with a steep SCO property. The complexes $[Fe(H_2L^{2\text{-}Me})_2]X\cdot Y\cdot$solvent (X = Cl, Br; Y = ClO_4, BF_4, PF_6, AsF_6; **2a**−**2d**, **2a′**, and **2a″**) have an isomorphous 2D network structure and show a variety of SCOs depending on the counteranion X, crystal solvent, and halide ion. The correlation between the structural parameters of the 2D complexes and the theoretical parameters is examined. $[Fe(H_2L^{2\text{-}Me})_2](BPh_4)_2\cdot CH_3CN$ (**3**) has no network structure, and $[Fe(H_2L^{2\text{-}Me})_2](ClO_4)_2$ (**4**) has a chiral 3D network structure, while **3** and **4** are HS complexes over the whole temperature range. Here, we report the syntheses, characterization, structures, and SCO properties of the family of iron(II) complexes. The study of **1** has been in part reported in a communication.[11]

Results and Discussion

Synthesis and Characterization of Iron(II) Complexes of (2-Methylimidazol-4-yl-methylidene)histamine, $[Fe(H_2L^{2\text{-}Me})_2]Cl_2\cdot 2\text{-PrOH}\cdot xH_2O$ (x = 0.5 (1) and x = 1 (1′)); $[Fe(H_2L^{2\text{-}Me})_2]Cl\cdot X\cdot EtOH$ (X = ClO_4 (2a), BF_4 (2b), PF_6 (2c), and AsF_6 (2d)); $[Fe(H_2L^{2\text{-}Me})_2]Cl\cdot ClO_4\cdot(1\text{-PrOH})\cdot 0.5H_2O$ (2a′) and $[Fe(H_2L^{2\text{-}Me})_2]Br\cdot ClO_4\cdot EtOH$ (2a″); $[Fe(H_2L^{2\text{-}Me})_2](BPh_4)_2\cdot MeCN$ (3); and $[Fe(H_2L^{2\text{-}Me})_2](ClO_4)_2$ (4). In this study, a tridentate ligand, (2-methylimidazol-4-yl-methylidene)histamine, abbreviated as $H_2L^{2\text{-}Me}$, was used for the syntheses of iron(II) complexes. The syntheses were carried out in an inert N_2 atmosphere, although the crystals of iron(II) complexes thus prepared are stable in air. The ligand was prepared by a 1:1 condensation reaction of 2-methyl-4-formylimidazole and histamine in ethanol or other solvents, and the ligand solution was used for the synthesis of iron(II) complexes without further purification. The 2:1 mixed solution of the ligand solution and $FeCl_2\cdot 4H_2O$ showed a thermochromism from yellow at room temperature to orange-red at lower temperatures, suggesting that the species $[Fe(H_2L^{2\text{-}Me})_2]^{2+}$ has a suitable ligand field strength near the SCO point and shows a SCO in solution. Using the complex species $[Fe(H_2L^{2\text{-}Me})_2]^{2+}$ and several anions, a family of iron(II) complexes with general chemical formulas of $[Fe(H_2L^{2\text{-}Me})_2]X_2\cdot$solvent (X = Cl, BPh_4, ClO_4) and $[Fe(H_2L^{2\text{-}Me})_2]X\cdot Y\cdot$solvent (X = Cl, Br; Y = ClO_4, BF_4, PF_6, AsF_6) were synthesized.

When a solution of $FeCl_2\cdot 4H_2O$ in 2-propanol (2-PrOH) and the ligand solution were mixed in 1:2 molar ratio, $[Fe(H_2L^{2\text{-}Me})_2]Cl_2\cdot 2\text{-PrOH}\cdot 0.5H_2O$ (**1**) was obtained as orange rhombic crystals. $[Fe(H_2L^{2\text{-}Me})_2]Cl_2\cdot 2\text{-PrOH}\cdot H_2O$ (**1′**) was obtained when a solution of an equimolar amount of NaBr in 2-PrOH was added to the mixed solution of the ligand and $FeCl_2\cdot 4H_2O$ in the hope of obtaining $[Fe(H_2L^{2\text{-}Me})_2]Cl\cdot Br\cdot n$solvent. Compounds **1** and **1′** showed a thermochromism in both the solid and solution states from orange at room temperature to red at liquid-nitrogen temperatures, suggesting SCO properties. Compound **1′** crystallized into a monoclinic centrosymmetric space group $P2_1/c$, while **1** crystallized into an orthorhombic acentrosymmetric space group $P2_12_12_1$. The quantities of the crystal solvents were confirmed by the thermogravimetric analyses. For **1**, the gradual weight loss corresponding to $0.5H_2O$ was observed from room temperature to 75 °C (348 K), and subsequently two-step weight losses corresponding to one 2-PrOH were observed at 75−120 °C and 120−180 °C. For **1′**, a rather abrupt one-step weight loss corresponding to the total molecular weight of one H_2O and one 2-PrOH was observed in the temperature region of 38−150 °C.

$[Fe(H_2L^{2\text{-}Me})_2]Cl\cdot ClO_4\cdot EtOH$ (**2a**) was obtained as orange rhombic crystals by mixing a solution of $FeCl_2\cdot 4H_2O$, the ligand solution, and a solution of $LiClO_4$ in ethanol in a 1:2:1 molar ratio at room temperature. When $LiBF_4$, KPF_6, and $NaAsF_6$ were used instead of $LiClO_4$, compounds $[Fe(H_2L^{2\text{-}Me})_2]Cl\cdot BF_4\cdot EtOH$ (**2b**), $[Fe(H_2L^{2\text{-}Me})_2]Cl\cdot PF_6\cdot EtOH$ (**2c**), and $[Fe(H_2L^{2\text{-}Me})_2]Cl\cdot AsF_6\cdot EtOH$ (**2d**) were similarly synthesized and obtained as well-grown orange crystals. $[Fe(H_2L^{2\text{-}Me})_2]Cl\cdot ClO_4\cdot 0.5(1\text{-PrOH})\cdot 0.5H_2O$ (**2a′**) was similarly prepared using 1-PrOH as the reaction solvent, in order to study the effect of the crystal solvent. $[Fe(H_2L^{2\text{-}Me})_2]Br\cdot ClO_4\cdot EtOH$ (**2a″**) was similarly prepared using $FeBr_2$ instead of $FeCl_2\cdot 4H_2O$, in order to study the effect of the bridging halogen ion. All of these compounds showed a thermochromism both in the solid and solution states from orange at room temperature to deep red at liquid nitrogen temperatures, suggesting SCO properties. The freshly prepared crystals were coated quickly with an epoxy resin and used for the X-ray diffraction studies. On the basis of the X-ray analyses, it was confirmed that the freshly prepared crystals of **2a**−**2d** and **2a″** involve one ethanol molecule per formula as the crystal solvents and the crystal of **2a′** involves one 1-PrOH and $0.5H_2O$. Their crystal solvents are partly eliminated under the open atmosphere to lose crystallinity gradually. The crystals were left for a few weeks in the open atmosphere at ambient temperatures until the sample weights showed no further change, and then the samples were used for the thermogravimetric analysis (TGA), elemental analysis, magnetic susceptibility measurements, and Mössbauer spectroscopy measurements. On heating the samples from room temperature, the TGA analysis showed no weight loss at least until 150 °C (423 K) and then showed the decrease of corresponding to the amounts of the

(11) Sato, T.; Iijima, S.; Kojima, M.; Matsumoto, N. *Chem. Lett.* **2009**, 178–179.

Table 1. Crystallographic Data for **1** and **1′**

complex	**1**	**1′**
formula	$C_{23}H_{35}N_{10}Cl_2O_{1.5}Fe$	$C_{23}H_{36}N_{10}Cl_2O_2Fe$
fw	602.35	611.36
space group	$P2_12_12_1$ (No.19)	$P2_1/c$ (No.14)
a, Å	9.130(2)	9.230(3)
b, Å	16.536(4)	19.820(7)
c, Å	19.866(4)	17.175(5)
β, deg		97.991(11)
V, Å^3	2999.1(12)	3111.5(16)
Z	4	4
T, K	296	296
D_{calcd}, g cm^{-3}	1.334	1.305
R, R_w[a]	0.0439, 0.0595	0.0541, 0.1829
Flack parameter	0.00(2)	

[a] $R = \sum||F_o| - |F_c||/\sum|F_o|$, $R_w = \{\sum[w(F_c^2 - F_c^2)^2]/\sum w(F_o^2)^2\}^{1/2}$.

crystal solvents. The quantities of ethanol of these samples were determined to be 0.5, 0.6, 0.8, and 0.9 for **2a**, **2b**, **2c**, and **2d**, respectively, and 0.5 for **2a″** per formula by their elemental analyses and TGA. The sample of **2a′** left in the air is consistent with the formula of $[Fe(H_2L^{2\text{-}Me})_2]Cl\cdot ClO_4\cdot 0.5(1\text{-}PrOH)\cdot 1.5H_2O$ on the basis of the elemental analysis, and the quantities of the solvents, $0.5(1\text{-}PrOH)\cdot 1.5H_2O$, were confirmed by the TGA analysis, in which the gradual loss corresponding to 1.5 H_2O molecules from room temperature to 100 °C (373 K) and subsequently the loss corresponding to half of a 1-PrOH molecule from 100 °C were observed.

To a mixed solution of $FeCl_2\cdot 4H_2O$ and the ligand solution in ethanol was added a solution of $NaBPh_4$ in ethanol. Soon after the addition of $NaBPh_4$, yellow-colored fine crystals precipitated. Recrystallization of the crude product from acetonitrile gave well-grown yellow crystals of $[Fe(H_2L^{2\text{-}Me})_2](BPh_4)_2\cdot MeCN$ (**3**). $[Fe(H_2L^{2\text{-}Me})_2](ClO_4)_2$ (**4**) was obtained as yellow rhombic crystals by mixing a solution of $Fe(ClO_4)_2\cdot 6H_2O$ and the ligand solution in ethanol in a 1:2 molar ratio. These two compounds, **3** and **4**, showed no thermochromism from room temperature to liquid nitrogen temperature in the solid state, while their solutions in acetonitrile and methanol showed thermochromism.

Crystal Structures of 1D Complexes $[Fe(H_2L^{2\text{-}Me})_2]Cl_2\cdot 2\text{-}PrOH\cdot 0.5H_2O$ (1) and $[Fe(H_2L^{2\text{-}Me})_2]Cl_2\cdot 2\text{-}PrOH\cdot H_2O$ (1′). The crystallographic data of **1** and **1′** are given in Table 1. Relevant bond distances and hydrogen-bond distances are given in Table 2. The coordination angles are given in Supporting Information S1. Both complexes have a similar 1D rodlike structure, but they crystallize in different crystal systems. An ORTEP drawing of **1** is shown in Figure 1. The iron(II) ion assumes an octahedral coordination environment with N_6 donor atoms of two unsymmetrical tridentate ligands. The complex cation is a chiral species due to octahedral coordination of two unsymmetrical tridentate ligands, as shown in Chart 1. The Fe−N bond distances are in the range of 2.133(4)−2.197(4) Å at 296 K, consistent with those of the HS Fe^{II} complexes with the N_6 donor atoms.[1a] All four imidazole groups of $[Fe(H_2L^{2\text{-}Me})_2]^{2+}$ are hydrogen-bonded to the Cl^- ions with hydrogen-bond distances of N(1)···Cl(1) = 3.123(5) Å, N(9)···Cl(2) = 3.172(4) Å, N(4)···Cl(1)* = 3.182(5) Å, and N(6)···Cl(2)* = 3.132(5) Å, where Cl(1)* and Cl(2)* represent the transformed atoms of Cl(1) and Cl(2), respectively. As a result of the repeating NH···Cl^- hydrogen bonds, the adjacent two complexes $[Fe(H_2L^{2\text{-}Me})_2]^{2+}$ are doubly bridged by two Cl^- ions of Cl(1) and Cl(2) through the four hydrogen bonds of NH(formylimidazole residue)···Cl^-···HN(histamine residue) to form a rodlike 1D structure, as shown in Figure 2. Within a rod, the adjacent two complexes $[Fe(H_2L^{2\text{-}Me})_2]^{2+}$ are related by a two-fold screw axis, and hence the iron(II) complexes with the same chirality are linked by the hydrogen bonds along the c axis to give a chiral rod. Compound **1′** assumes a similar rodlike 1D structure, and the coordination bond and hydrogen distances are compatible with those of **1**, as shown in Table 2.

Table 2. Relevant Coordination Bond Lengths (Å) and Hydrogen Bond Lengths (Å) for **1** and **1′** at 296 K[a]

complex	**1**	**1′**
Fe(1)−N(2)	2.191(4)	2.181(3)
Fe(1)−N(3)	2.176(4)	2.216(3)
Fe(1)−N(5)	2.133(4)	2.126(3)
Fe(1)−N(7)	2.197(4)	2.189(3)
Fe(1)−N(8)	2.179(4)	2.193(3)
Fe(1)−N(10)	2.153(4)	2.152(3)
	Hydrogen Bonds	
N(1)···Cl(1)	3.123(5)	3.191(4)
N(9)···Cl(2)	3.172(4)	3.141(4)
N(4)···Cl(1)	3.182(5)*	3.173(3)**
N(6)···Cl(2)	3.132(5)*	3.148(4)**
O(2)···Cl(1)	3.221(10)	3.234(4)
O(1)···Cl(2)	3.092(6)	3.114(9)***
O(2)···Cl(1)	3.344(10)****	3.318(5)*****

[a] Symmetry operations: (*) $-x+1/2, -y+1, z+1/2$. (**) $-x+1, y+1/2; -z+1/2$. (***) $-x, -y+1, -z$. (****) $x+1/2, -y+1/2+1, -z$. (*****) $-x, -y+1, -z+1$.

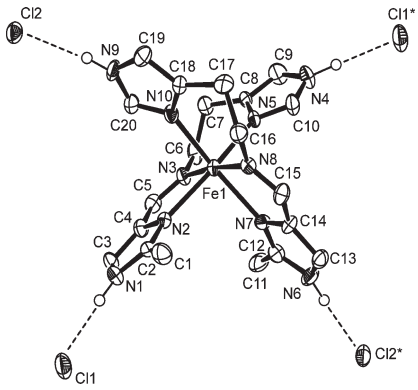

Figure 1. An ORTEP drawing of a complex cation, $[Fe(H_2L^{2\text{-}Me})_2]^{2+}$, and the hydrogen-bonded four adjacent Cl^- ions of $[Fe(H_2L^{2\text{-}Me})_2]Cl_2\cdot 2\text{-}PrOH\cdot 0.5H_2O$ (**1**), together with the atom numbering scheme. Due to the configuration of two unsymmetrical tridentate ligands around iron(II), the complex cation is a chiral species. The hydrogen atoms except for four hydrogen atoms bonded to four imidazole nitrogen atoms are omitted for clarity. The atoms of Cl(1)* and Cl(2)* are the symmetry-translated atoms, where * denotes the symmetry operation of $-x+1/2, -y+1, z+1/2$.

As **1** crystallized into an acentrosymmetric space group $P2_12_12_1$ and **1′** crystallized into a centrosymmetric space group $P2_1/c$, the crystal packings of the 1D rods are different from each other. The crystal packing diagrams of the 1D rods are shown in Figures 3 and 4 for **1** and **1′**, respectively. As shown in Figures 3a and 4a, adjacent 1D

rods having the same chirality are stacked in a crystal lattice, resulting in a chiral crystal (racemic mixture, conglomerate) for **1**, while adjacent 1D rods with the opposite chiralities are alternately arrayed to give an achiral crystal (racemic compound) for **1′**. Crystal solvent 2-PrOH is hydrogen-bonded to one of two Cl^- ions with O(1)···Cl(2) = 3.092(6) Å for **1** and O(1)···Cl(2) = 3.114(9) Å for **1′**. The most striking difference between **1** and **1′** is found in the orientation of 2-PrOH, as seen in Figures 3b and 4b. As shown in Figures 3c and 4c, it is apparent that the crystal solvents play an important role in the different packings of the 1D rods. The water molecule of the crystal solvent is hydrogen-bonded to another Cl^- ion with O(2)···Cl(1) = 3.221(10) Å for **1** and O(2)···Cl(1) = 3.234(4) Å for **1′**. In addition, the water molecule is weakly hydrogen-bonded to the Cl(1) of the adjacent 1D rod to link the 1D rods two-dimensionally, where the O···Cl^- distances are 3.344(10) and 3.318(5) Å for **1** and **1′**, respectively.

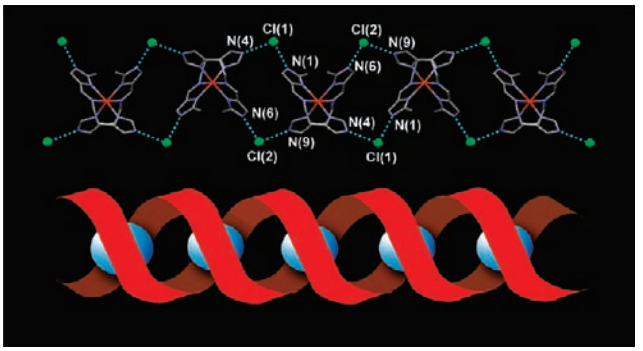

Figure 2. Chiral rodlike 1D structure of $[Fe(H_2L^{2\text{-}Me})_2]Cl_2\cdot$2-PrOH$\cdot$0.5$H_2O$ (**1**). Complex **1′** assumes a similar rodlike 1D structure along the *c* axis. (Top) Two adjacent complex cations, $[Fe(H_2L^{2\text{-}Me})_2]^{2+}$, are doubly bridged by two Cl^- ions (Cl(1) and Cl(2)) through NH···Cl^- hydrogen bonds, giving a chiral rodlike structure, where the crystal solvents and hydrogen atoms are omitted for clarity. (Bottom) Schematic drawing of a chiral rodlike 1D structure.

Circular Dichroism Spectra of $[Fe(H_2L^{2\text{-}Me})_2]Cl_2\cdot$2-PrOH$\cdot$0.5$H_2O$ (1). To confirm the conglomerate crystallization of **1**, the circular dichromism (CD) spectra were measured in the range of 350−600 nm, and they are shown in Figure 5. One crystallite showed a positive and a negative CD peak at 450 and 595 nm (red curve), and the spectrum of another crystallite showed an enantiomeric CD pattern (black curve). The enantiomeric CD spectra obtained from selected crystallites provided definitive evidence that spontaneous resolution took place during the course of crystallization.

SCO of 1D Complexes $[Fe(H_2L^{2\text{-}Me})_2]Cl_2\cdot$2-PrOH$\cdot$0.5$H_2O$ (1) and $[Fe(H_2L^{2\text{-}Me})_2]Cl_2\cdot$2-PrOH$\cdot H_2O$ (1′). The general procedure for the magnetic susceptibility measurements is as follows: The powdered samples were quickly cooled from room temperature to 5 K within a few seconds, and the magnetic susceptibility was first

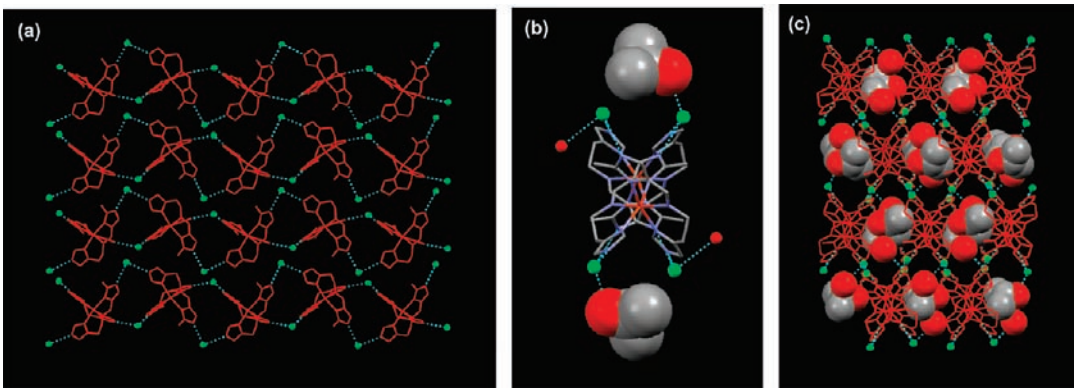

Figure 3. Crystal structure of **1**. (a) Adjacent 1D rods with the same chirality are stacked in a crystal lattice to give a chiral crystal (conglomerate). (b) Projection along the rodlike 1D chain, showing the orientation of 2-PrOH molecules, which are hydrogen-bonded to Cl^- ions. (c) Side view of 1D rods along the *c* axis, showing that the adjacent rods are stacked and the solvents are positioned in the square consisting of four rods.

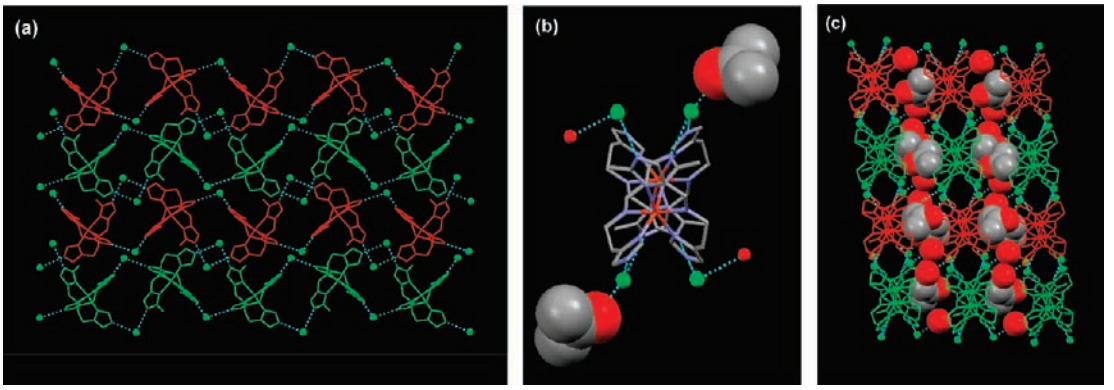

Figure 4. Crystal structure of **1′**. (a) Adjacent 1D rods with the opposite chiralities running along the *b* axis are alternately stacked in a crystal lattice to give an achiral crystal packing (racemic compound), where two enantiomorphs are drawn in green and red. (b) Projection along the 1D rod, showing the orientation of 2-PrOH molecules which were hydrogen-bonded to Cl^- ions. (c) Side view of 1D rods along the *b* axis, showing that the adjacent rods are stacked and the solvents are positioned at layers consisting of rods with the opposite chirality.

measured upon warming from 5 to 350 K (first run) and then measured upon cooling from 350 to 5 K (second run) at a 1 K min^{-1} sweep rate under a 0.5 T applied magnetic field by the use of a SQUID magnetometer.

Figure 6 shows the $\chi_M T$ versus T plots of **1**. For the first run of the hemihydrated sample (**1**), the $\chi_M T$ versus T plots showed a frozen-in-effect and an incomplete two-step SCO behavior. TGA revealed that, at 350 K, which is the final temperature of the first run, $0.5H_2O$ is eliminated

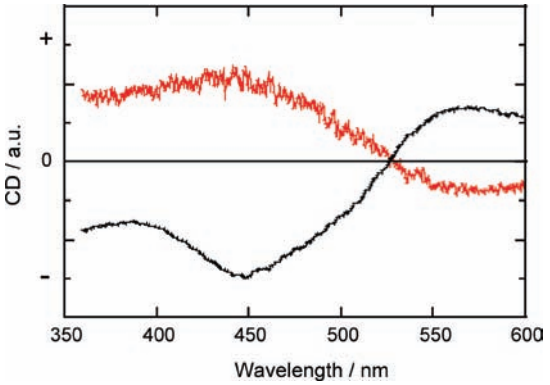

Figure 5. CD spectra of crystallites of **1** in KBr pellets. The two KBr pellets prepared from two different crystals showed enantiomeric CD patterns (red versus black curve).

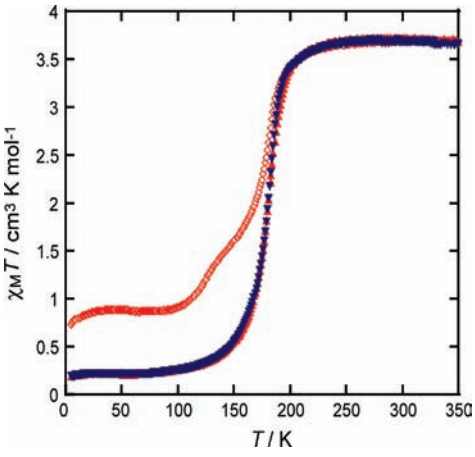

Figure 6. The $\chi_M T$ vs T plots of $[Fe(H_2L^{2\text{-}Me})_2]Cl_2 \cdot 2\text{-PrOH} \cdot 0.5H_2O$ (**1**), showing a two-step SCO for the hydrated sample (first run, red ◊) and an abrupt one-step SCO for the dehydrated sample (second and third runs, blue ▼ and red ▲).

while 2-PrOH remained to form $[Fe(H_2L^{2\text{-}Me})_2]Cl_2 \cdot$ 2-PrOH. In the second run and the subsequent run, the $\chi_M T$ versus T plots showed a reversible steep one-step SCO without hysteresis, in which the $\chi_M T$ value in the region of 350−200 K was ca. 3.7 cm^3 K mol^{-1} (typical value for HS Fe^{II} state) and steeply decreased from ca. 3.7 cm^3 K mol^{-1} at 200 K to 0.2 cm^3 K mol^{-1} at 100 K (a slightly large value for the LS Fe^{II} state), and the inflection point was evaluated to be 180 K. To confirm the solvent effect, the third run was carried out from 5 to 350 K in the warming mode, showing no difference from second run. The steep one-step SCO can be ascribed to intermolecular interaction within a 1D rod. The incomplete two-step SCO of the hydrated sample can be ascribed to a 2D network, because the water molecule bridges adjacent 1D rods through the hydrogen bonds of $O \cdots Cl^-$ to give a 2D network structure.

Crystal Structures in the HS States of 2D Complexes $[Fe(H_2L^{2\text{-}Me})_2]Cl \cdot X \cdot EtOH$ (X = ClO_4 (2a), BF_4 (2b), PF_6 (2c), and AsF_6 (2d)) and $[Fe(H_2L^{2\text{-}Me})_2]Cl \cdot ClO_4 \cdot (1\text{-PrOH}) \cdot 0.5H_2O$ (2a′). Complexes **2a**−**2d**, **2a**′, and **2a**″ have an isomorphous structure, and the same atom numberings except for those of the counteranion X and the crystal solvents are taken throughout **2a**−**2d**, **2a**′, and **2a**″. Crystallographic data of the chloride complexes **2a**−**2d** and **2a**′ are given in Table 3. Their relevant bond distances and hydrogen-bond distances are summarized in Table 4. The coordination angles are given in Supporting Information S2.

The structure of the ClO_4 salt (**2a**) is exemplified in detail, as **2a**−**2d**, **2a**′, and **2a**″ have an isomorphous structure. Figure 7 shows an ORTEP drawing of **2a**, representing the coordination geometry and hydrogen bonds around complex cation $[Fe(H_2L^{2\text{-}Me})_2]^{2+}$. The iron(II) ion has octahedral coordination geometry with N_6 donor atoms of two tridentate ligands. In the octahedron, each tridentate ligand $H_2L^{2\text{-}Me}$ with unsymmetrical N_3 donor atoms takes a meridional configuration, and hence the Fe^{II} complex coordinated by the two ligands becomes a chiral molecule. The Fe−N bond distances of **2a** are in the range of 2.143(5)−2.189(6) Å, consistent with those of the high-spin Fe^{II} complexes with similar N_6 donor atoms at 296 K.[1a] As shown in Figure 7, two formylimidazole moieties and one histamine moiety of four imidazole groups per complex molecule are hydrogen-bonded to their nearest Cl^- ions with hydrogen-bond

Table 3. Crystallographic Data for **2a**−**2d** and **2a**′

complex	**2a**	**2b**	**2c** (296 K)	**2c** (120 K)	**2d** (296 K)	**2d** (110 K)	**2a**′
formula	$C_{22}H_{32}N_{10}Cl_2O_5Fe$	$C_{22}H_{32}N_{10}BF_4ClOFe$	$C_{22}H_{32}N_{10}PF_6ClOFe$	$C_{22}H_{32}N_{10}PF_6ClOFe$	$C_{22}H_{32}N_{10}AsF_6ClOFe$	$C_{22}H_{32}N_{10}AsF_6ClOFe$	$C_{23}H_{35}N_{10}Cl_2O_{5.5}Fe$
fw	643.31	630.66	688.83	688.83	732.77	732.77	672.33
space group	$P2_1/n$ (No. 14)	$P2_1/n$ (No. 14)	$P2_1/n$ (No. 14)	$P2_1/n$ (No. 14)	$P2_1/n$ (No. 14)	$P2_1/n$ (No. 14)	$P2_1/n$ (No. 14)
a, Å	12.059(5)	11.943(3)	11.965(4)	11.876(4)	11.916(4)	11.802(4)	12.282(6)
b, Å	19.048(9)	18.921(5)	19.257(7)	18.705(7)	19.428(6)	18.701(6)	19.358(6)
c, Å	13.079(5)	13.082(4)	13.344(6)	13.013(6)	13.381(4)	13.242(5)	12.971(5)
β, deg	95.132(14)	95.159(11)	96.297(14)	95.053(17)	96.671(14)	95.864(17)	96.408(16)
V, Å^3	2992.0(20)	2944.2(14)	3056(2)	2879(2)	3076.7(17)	2907.3(17)	3064.5(20)
Z	4	4	4	4	4	4	4
T, K	296	296	296	120	296	110	296
D_{calcd}, g cm^{-3}	1.426	1.423	1.497	1.589	1.582	1.674	1.444
R, R_w[a]	0.0537, 0.1398	0.0594, 0.1628	0.0747, 0.1927	0.0699, 0.1706	0.0610, 0.1716	0.0435, 0.1196	0.0569, 0.1629

[a] $R = \sum||F_o| - |F_c||/\sum|F_o|$; $R_w = \{\sum[w(F_c^2 - F_c^2)^2]/\sum w(F_o^2)^2\}^{1/2}$.

Table 4. Relevant Coordination Bond Lengths (Å), Angles (deg), and Hydrogen Bond Lengths (Å) for **2a**−**2d** and **2a′**[a]

complex	**2a**	**2b**	**2c** (296 K)	**2c** (120 K)	**2d** (296 K)	**2d** (110 K)	**2a′**
Fe(1)−N(2)	2.173(6)	2.167(5)	2.184(5)	2.012(5)	2.208(5)	1.998(2)	2.184(4)
Fe(1)−N(3)	2.189(6)	2.177(5)	2.180(5)	1.977(5)	2.179(5)	1.982(2)	2.191(5)
Fe(1)−N(5)	2.143(5)	2.135(5)	2.143(5)	1.994(5)	2.154(5)	1.998(2)	2.139(4)
Fe(1)−N(7)	2.153(5)	2.164(4)	2.177(5)	1.994(5)	2.193(5)	2.015(2)	2.170(4)
Fe(1)−N(8)	2.183(5)	2.189(5)	2.172(6)	1.990(5)	2.192(5)	1.977(2)	2.191(4)
Fe(1)−N(10)	2.148(5)	2.144(4)	2.148(5)	2.005(5)	2.153(5)	2.002(2)	2.132(4)
			Hydrogen Bond				
N(1)···Cl* or Br	3.299(8)	3.235(7)	3.367(7)	3.380(6)	3.373(7)	3.115(2)	3.431(9)
N(4)···Cl** or Br	3.252(8)	3.238(6)	3.326(7)	3.218(6)	3.363(6)		3.305(6)
N(6)···Cl or Br	3.181(7)	3.149(6)	3.130(7)	3.156(6)	3.125(6)	3.312(3)	3.110(5)
N(9)···Cl						3.227(3)	
N(9)···O(1) or F(1)***	2.975(9)	2.898(7)	2.942(12)	2.958(9)	2.975(11)		2.984(6)
O···Cl			3.215(9)	3.215(7)	3.192(8)		
O(5)···O(6)****							2.66(2)

[a] Symmetry operations: (*) $1/2 - x, 1/2 - y, 1/2 - z$. (**) $-x+1, -y+1, -z+1$. (***) $x+1, y, z$. (****) $-x+1/2+1, y+1/2-1, -z+1/2$. (*****) $-x+2, -y+1, -z+1$.

distances of N(1)···Cl(1)* = 3.299(8) Å, N(4)···Cl(1)** = 3.252(8) Å, and N(6)···Cl(1) = 3.181(7) Å, where Cl(1)* and Cl(1)** represent the Cl(1) atoms transformed by the symmetry operations of $(1/2 - x, 1/2 - y, 1/2 - z)$ and $(1-x, 1-y, 1-z)$, respectively. The remaining histamine moiety is hydrogen-bonded to an oxygen atom of the ClO_4^- ion with a hydrogen-bond distance of N(9)···O(1)*** = 2.975(9) Å, where the O(1)*** atom is the atom translated by a symmetry operation of $(x+1, y, z)$.

Figure 8a shows the 2D network structure of **2a**, where the anion ClO_4^- is not involved in the formation of the 2D network and thus is omitted for clarity. The 2D network structure is constructed by the three NH···Cl^- hydrogen bonds, where the chloride ion Cl(1) plays the role of a connector. The 2D network structure consists of two types of units, a cyclic dinuclear net of $\{[Fe(H_2L^{2\text{-}Me})_2]\text{-}Cl\}_2$ and a cyclic tetranuclear net of $\{[Fe(H_2L^{2\text{-}Me})_2]Cl\}_4$. These two types of nets are oriented nearly perpendicular to each other and arrayed alternately to give the 2D network, where the ethanol molecule as the crystal solvent is positioned in a cavity of cyclic dinuclear net $\{[Fe(H_2L^{2\text{-}Me})_2]Cl\}_2$. Figure 8b shows a side view of a adjacent 2D layer, where the ClO_4^- anions are attached to an undulated layer of a 2D network with a hydrogen bond of N(9)···O(1)*** = 2.975(9) Å from the upper and lower sides, and the ethanol molecule as the crystal solvent is represented by a space filling model. Figure 8c shows a side view of two adjacent 2D layers, where the anion ClO_4^- is represented by a space filling model. The anions ClO_4^- are hydrogen-bonded to an undulated layer of a 2D network from the upper and lower sides. The resulting undulated ClO_4^- layer occupies and adapts the space between the undulated layers of 2D layers $\{[Fe(H_2L^{2\text{-}Me})_2]Cl\}_n$. The complex cation is a chiral species due to octahedral coordination of two unsymmetrical tridentate ligands. Since the 2D complexes are crystallized into centrosymmetric space group $P2_1/n$, two enantiomorphs exist in a crystal. Figure 8d shows a 2D network structure consisting of two alternately arrayed enantiomorphs (green and red molecules). In either of the component nets, a cyclic dinuclear net of $\{[Fe(H_2L^{2\text{-}Me})_2]Cl\}_2$ and a cyclic tetranuclear net of $\{[Fe(H_2L^{2\text{-}Me})_2]Cl\}_4$, two enantiomorphs are alternately linked by hydrogen bonds.

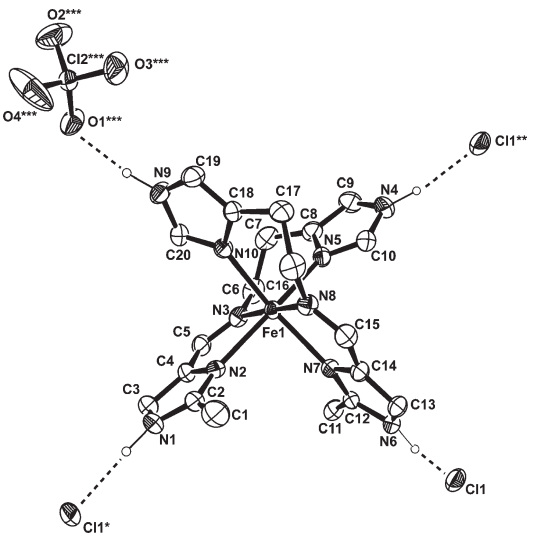

Figure 7. An ORTEP drawing of a complex cation, $[Fe(H_2L^{2\text{-}Me})_2]^{2+}$, and the hydrogen-bonded three adjacent Cl^- ions and one ClO_4^- ion of $[Fe(H_2L^{2\text{-}Me})_2]Cl\cdot ClO_4\cdot EtOH$ (**2a**), together with the atom numbering scheme. Due to the meridional configurations of two unsymmetrical tridentate ligands, the complex cation is a chiral molecule. The hydrogen atoms except for four hydrogen atoms bonded to four imidazole nitrogen atoms are omitted for clarity. The atoms of Cl1* and Cl1** are the symmetry-translated atoms of Cl1, where * and ** denote the symmetry operations of $(1/2 - x, 1/2 - y, 1/2 - z)$ and $(1 - x, 1 - y, 1 - z)$, respectively.

As the crystal structures of 2D complexes **2a**−**2d**, **2a′**, and **2a″** are isomorphous to each other, hereafter the notable structural features of **2b**−**2d**, **2a′**, and **2a″** are described. The Fe−N bond distances of all of these complexes are compatible with those of the high-spin Fe^{II} complexes with similar N_6 donor atoms at 296 K.[1a] Similarly to **2a**, three imidazole groups of the complex cation of **2b**−**2d**, **2a′**, and **2a″** are hydrogen-bonded to Cl^- (or Br^-) ions to form a 2D network structure, though the three NH···Cl^- distances show a remarkable difference depending on the compounds. For the chloride complexes **2a**−**2d** and **2a′**, the N(6)···Cl does not show a big difference, but N(1)···Cl* and N(4)···Cl** show a remarkable elongation in **2c**, **2d**, and **2a′**. The remaining histamine group of four imidazole groups is hydrogen-bonded to F (or O) atoms of the anion (BF_4^-, PF_6^-,

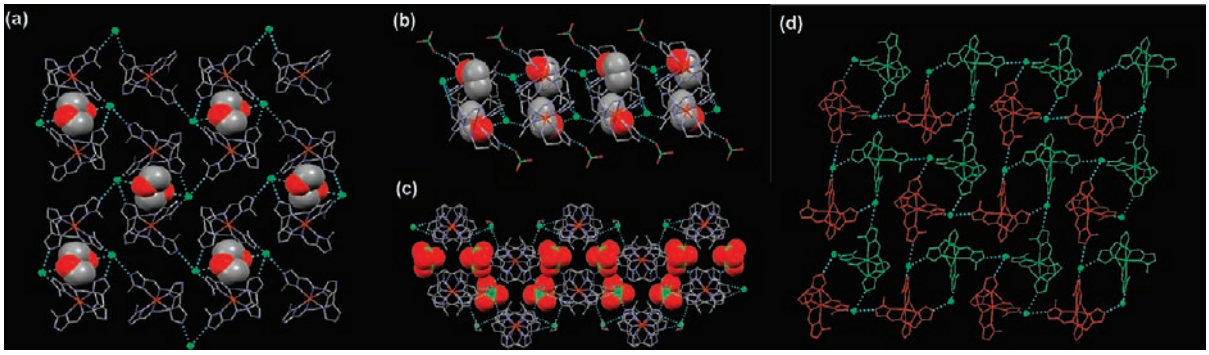

Figure 8. Hydrogen-bonded 2D network structure of $[Fe(H_2L^{2\text{-}Me})_2]Cl\cdot ClO_4\cdot EtOH$ (**2a**). (a) A 2D network structure constructed by the NH···Cl^- hydrogen bonds, where the anion ClO_4^- is omitted for clarity. One Cl^- ion (green) is hydrogen-bonded to three imidazole NH groups of three $[Fe(H_2L^{2\text{-}Me})_2]^{2+}$'s to give the 2D network structure. The crystal solvents drawn by the space filling model are positioned in a cavity of the 2D layer. (b) Side view of a 2D layer along the *b* axis, showing that solvents are positioned in a layer and ClO_4^- anions are hydrogen-bonded to a 2D layer from upper and lower sides. (c) Stacking of the adjacent two puckered 2D layers. The counteranions drawn by the space filling model occupy the space between the puckered layers. (d) A 2D network structure consists of two alternately arrayed enantiomorphs (green and red molecules).

SbF_6^-, ClO_4^-) with hydrogen bond distances of N(9)···F(1)*** = 2.898(7) Å for **2b**, N(9)···F(1)***=2.942(12) Å for **2c**, N(9)···F(1)*** = 2.975(11) Å for **2d**, and N(9)···O(1)*** = 2.984(6) Å for **2a′**. For **2a″**, the corresponding distance of N(9)···O(1)*** = 3.308(17) Å is elongated and too long for a hydrogen bond. Among the anions (BF_4^-, PF_6^-, SbF_6^-, ClO_4^-) of **2a**−**2d**, **2a′**, and **2a″**, only the AsF_6 anion showed a disorder at 296 K due to the rotation motion. The crystal solvents of **2a**, **2b**, **2a′**, and **2a″** have no hydrogen bonds to the 2D network and are just accommodated in the cavity. On the other hand, those of **2c** and **2d** are hydrogen-bonded to the chloride ion OH···Cl(1) with hydrogen bond distances of 3.215(9) and 3.192(8) Å, respectively. 1-PrOH of **2a′** is accommodated in the cavity of the 2D net, and H_2O is hydrogen-bonded to the 1-PrOH molecule with O(5)···O(6)****=2.66(2) Å, where O(6)**** represents the O(6) atom transformed by the symmetry operation of $(-x + 1/2 + 1, y + 1/2-1, -z + 1/2)$.

Structures in the LS States of $[Fe(H_2L^{2\text{-}Me})_2]Cl\cdot PF_6\cdot EtOH$ (2c) at 120 K and $[Fe(H_2L^{2\text{-}Me})_2]Cl\cdot AsF_6\cdot EtOH$ (2d) at 110 K. As later described, the magnetic susceptibilities and Mössbauer spectra demonstrated that **2c** and **2d** showed a reversible, steep one-step SCO from the HS to the LS state. Their crystal structures in the LS state were determined by a single-crystal X-ray diffraction analysis, and the results are given in Tables 3 and 4. As evidenced by the crystallographic data of Table 3, **2c** and **2d** assume an isomorphous structure in the HS and LS states, which consists of one molecular unit as a crystallographic unique unit and the same space group, $P2_1/n$, suggesting no phase transition during the SCO. The cell volume changes from 3056(2) Å^3 at 296 K to 2879(2) Å^3 at 120 K for **2c** and from 3076.7(17) Å^3 at 296 K to 2907.3(17) Å^3 at 110 K for **2d**, showing 5.8% and 5.5% volume reduction, respectively. All *a*, *b*, and *c* unit cell lengths decrease during the SCO from the HS to LS state, where *b* decreases the most. While the Fe^{II} ion assumes an octahedral coordination environment with the N_6 donor atoms, the Fe−N bond distances are in the range of 2.143(5)−2.184(5) Å at 296 K and 1.977(5)−2.012(5) Å at 120 K for **2c**. The N−Fe−N bond angles change to a regular octahedron at 120 K. A similar trend is observed for **2d**. These data are in accord with the typical spin transition of $Fe^{II}N_6$ chromospheres. Associated with the volume change of the Fe^{II} complex during the spin transition, several intermolecular hydrogen bonds show a noteworthy change. For **2c**, at 296 K, three N···Cl^- hydrogen-bond distances, N(6)···Cl, N(4)···Cl, and N(1)···Cl, are 3.130(7), 3.326(7), and 3.367(7) Å, while at 120 K, these are 3.156(6), 3.218(6), and 3.380(6). For **2d**, at 296 K, three N···Cl^- hydrogen bond distances, N(6)···Cl, N(4)···Cl, and N(1)···Cl, are 3.125(6), 3.363(6), and 3.373(7) Å, while at 110 K, the new hydrogen bonded structure around Cl^- ion is reconstructed and N(1)···Cl of 3.115(2) Å becomes the shortest. For **2c** and **2d**, one of three N···Cl^- distances is the extremely short and the other two are rather long. It should be noted that the AsF_6 anion of **2d** was disordered at 296 K due to the rotational motion, but the disorder disappeared at 110 K. Figure 9 shows the superimposed crystal structures of the HS and LS states of **2c**, showing the structural change during the spin transition from the HS to the LS state.

Magnetic Properties of 2D Complexes $[Fe(H_2L^{2\text{-}Me})_2]Cl\cdot X\cdot n$EtOH (X = ClO_4 (2a), BF_4 (2b), PF_6 (2c), and AsF_6 (2d)), $[Fe(H_2L^{2\text{-}Me})_2]Cl\cdot ClO_4\cdot 0.5$(1-PrOH)$\cdot 1.5H_2O$ (2a′), and $[Fe(H_2L^{2\text{-}Me})_2]Br\cdot ClO_4\cdot 0.5$EtOH (2a″). SCO of $[Fe(H_2L^{2\text{-}Me})_2]Cl\cdot ClO_4\cdot 0.5$EtOH (2a). The SCO behavior of the ClO_4 salt (**2a**) was shown in Figure 10. The magnetic behavior during the warming and cooling modes is similar except below 65 K. The difference below 65 K can be ascribed to the frozen-in effect. Compound **2a** showed no thermal hysteresis. For the first run in the warming mode, the $\chi_M T$ value of ca. 0.8 cm^3 K mol^{-1} at 5 K, considerably larger than the LS Fe^{II} value ($\chi_M T$ = 0 cm^3 K mol^{-1} expected for $S = 0$), increases a little to 0.9 cm^3 K mol^{-1}, assumes a constant value in the temperature region of ca. 20−40 K, decreases from ca. 0.9 cm^3 K mol^{-1} at 40 K to 0.4 cm^3 K mol^{-1} at 64 K, then begins to increase to reach a stable intermediate state of (HS + LS)/2 Fe^{II} in the region of 100−200 K, and finally abruptly increases to 3.3 cm^3 K mol^{-1} (a value for the HS Fe^{II} state). For the second run, upon lowering the temperature from 350 to 5 K, the $\chi_M T$ value of ca. 3.3 cm^3 K mol^{-1} in the region of 350−270 K (typical value for HS Fe^{II} state) was obtained, and the value moderately decreased from ca. 3.3 cm^3 K mol^{-1} at 270 K to 1.7 cm^3 K mol^{-1} at 200 K to reach a plateau value for the (HS + LS)/2 Fe^{II} state in the region of 200−100 K

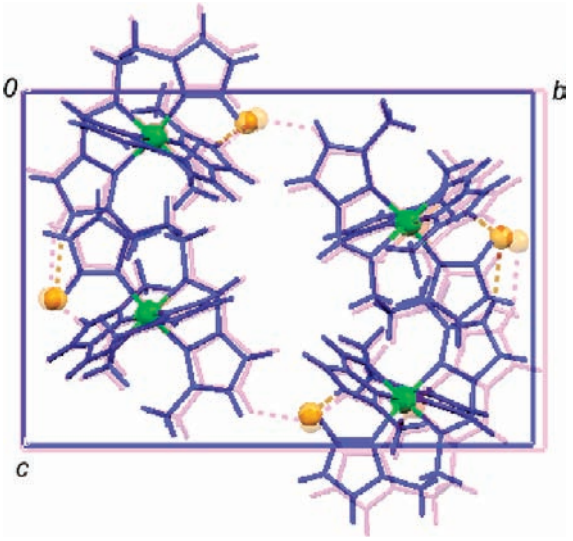

Figure 9. Superimposed crystal structure of the LS states on that of the HS states of **2c** projected on the *bc* plane, showing the structural change in a unit cell during the spin transition from the HS to LS state, where the anions and crystal solvents are omitted for clarity. The HS and LS molecules are drawn in pale red and blue, respectively. The HS and LS Fe^{II} ions are drawn as red and green balls, respectively.

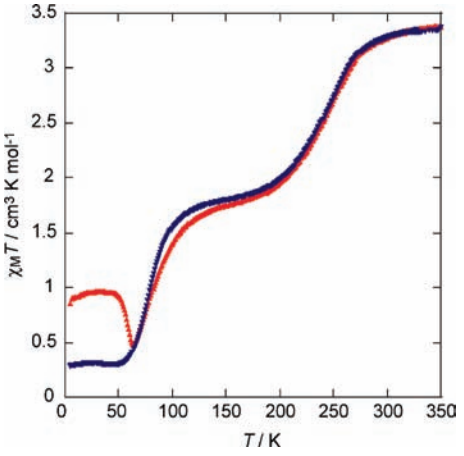

Figure 10. Magnetic behavior of $[Fe(H_2L^{2\text{-}Me})_2]Cl\cdot ClO_4\cdot 0.5EtOH$ (**2a**) in the form of the $\chi_M T$ versus T plots. The sample was warmed from 5 to 350 K (red ▲) and then cooled from 350 to 5 K (blue ▼) at a sweep rate of 1 K min^{-1}.

and finally abruptly decreased to give 0.3 cm^3 K mol^{-1} (a slightly large value for the LS Fe^{II} state), where the inflection points were evaluated to be $T_{1/2,2} = 255$ and $T_{1/2,1} = 75$ K for a SCO of HS ↔ (HS + LS)/2 and (HS + LS)/2 ↔ LS, respectively, demonstrating a wide temperature range for the intermediate spin state of (HS+LS)/2. Consequently, the width δT_C=180 K. A two-step SCO of the ClO_4 salt (**2a**) is noticeable since it shows one of the largest δT values.

Representative Mössbauer spectra of **2a** are shown in Figure 11. On increasing the temperature of the sample after rapid cooling to 4.2 K over several minutes, spectra were recorded at 4.2, 40, 78, 100, 130, 170, 200, 230, 250, 270, and 298 K. At 4.2 K, the spectrum consists of two doublets attributable to the HS Fe^{II} (δ=1.12 mm s^{-1}, ΔE_Q= 1.86 mm s^{-1}) and LS Fe^{II} species (δ=0.54 mm s^{-1}, ΔE_Q= 0.22 mm s^{-1}), with relative areas of 0.25 and 0.75. On increasing the temperature from 4.2 K, the relative intensity

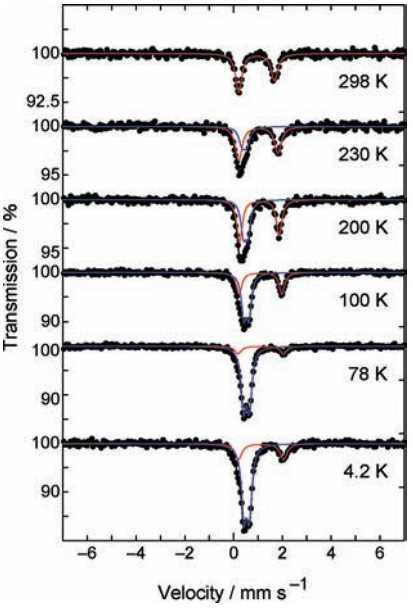

Figure 11. Selected ^{57}Fe Mössbauer spectra of $[Fe(H_2L^{2\text{-}Me})_2]Cl\cdot ClO_4\cdot 0.5EtOH$ (**2a**) recorded at 4.2, 78, 100, 200, 230, and 298 K in the warming mode after rapid cooling to 4.2 K. The HS and LS spectra generated by the deconvolution analyses are drawn in red and blue, respectively.

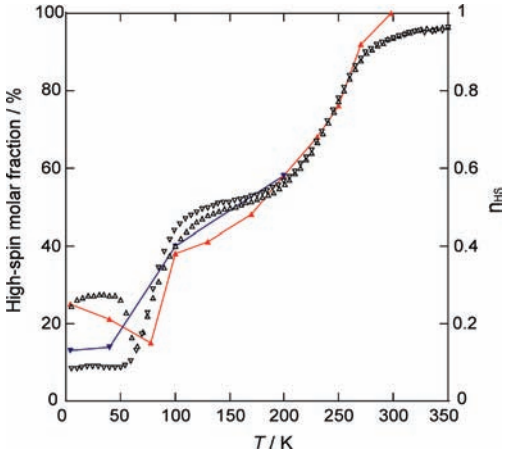

Figure 12. Molar fraction of HS versus total Fe^{II} for $[Fe(H_2L^{2\text{-}Me})_2]Cl\cdot ClO_4\cdot 0.5EtOH$ (**2a**) in the warming (red ▲) and cooling (blue ▼) modes obtained by deconvolution analysis of the Mössbauer spectra, together with the molar fraction n_{HS} obtained from the magnetic susceptibility measurements, where n_{HS} was calculated by using the equation $(\chi_M T)_{obs} = n_{HS}\ (\chi_M T)_{HS} + (1 - n_{HS})\ (\chi_M T)_{LS}$, with $(\chi_M T)_{HS}$ = 3.5 cm^3 K mol^{-1} and $(\chi_M T)_{LS}$=0.0 cm^3 K mol^{-1} as limiting values.

of the doublet due to the HS state decreases from 0.25 at 4.2 K to 0.15 at 78 K and then increases and reaches the 100% HS state, in the course of which an intermediate HS+LS state is observed in the range of 130−200 K, showing a steep two-step SCO behavior as well as the frozen-in effect. During slow cooling of the sample from 298 to 4.2 K, Mössbauer spectra were recorded at 200, 100, 40, and 4.2 K. At 200 K, the spectrum consists of two doublets attributable to the HS Fe^{II} (δ=1.05 mm s^{-1}, ΔE_Q=1.63 mm s^{-1}) and LS Fe^{II} species (δ = 0.49 mm s^{-1}, ΔE_Q = 0.19 mm s^{-1}), with relative areas of 0.58 and 0.42. On lowering the temperature from 200 K, the relative intensity of the doublet due to the HS state decreases, while that of the doublet due to the LS state increases. Finally, at 4.2 K, the spectrum consists of two doublets attributable to the HS

Table 5. Mössbauer Parameters for $[Fe(H_2L^{2\text{-Me}})_2]Cl\cdot ClO_4\cdot 0.5EtOH$ (**2a**)

On Heating after Rapid Cooling down to 4.2 K					
temp/K	δ^a/mm s^{-1}	ΔE_Q/mm s^{-1}	Γ^b/mm s^{-1}	area ratio/%	assignment
298	0.94	1.47	0.31	100	HS Fe^{II}
270	0.96	1.50	0.37	92	HS Fe^{II}
	0.37	0.19	0.29	8	LS Fe^{II}
250	1.02	1.56	0.33	76	HS Fe^{II}
	0.37	0.18	0.29	24	LS Fe^{II}
230	1.01	1.60	0.33	68	HS Fe^{II}
	0.44	0.19	0.29	33	LS Fe^{II}
200	1.06	1.63	0.27	58	HS Fe^{II}
	0.49	0.19	0.24	42	LS Fe^{II}
170	1.05	1.68	0.24	48	HS Fe^{II}
	0.49	0.19	0.24	52	LS Fe^{II}
130	1.10	1.71	0.25	41	HS Fe^{II}
	0.50	0.20	0.28	59	LS Fe^{II}
100	1.10	1.76	0.27	38	HS Fe^{II}
	0.52	0.21	0.24	62	LS Fe^{II}
78	1.11	1.87	0.31	15	HS Fe^{II}
	0.53	0.24	0.24	85	LS Fe^{II}
40	1.12	1.93	0.34	21	HS Fe^{II}
	0.53	0.22	0.25	79	LS Fe^{II}
4.2	1.12	1.86	0.34	25	HS Fe^{II}
	0.54	0.22	0.24	75	LS Fe^{II}
On Slow Cooling from Room Temperature					
temp/K	δ^a/mm s^{-1}	ΔE_Q/mm s^{-1}	Γ^b/mm s^{-1}	area ratio/%	assignment
200	1.05	1.63	0.28	58	HS Fe^{II}
	0.49	0.19	0.25	42	LS Fe^{II}
100	1.09	1.74	0.26	40	HS Fe^{II}
	0.52	0.20	0.24	60	LS Fe^{II}
40	1.12	1.92	0.30	14	HS Fe^{II}
	0.54	0.22	0.23	86	LS Fe^{II}
4.2	1.11	1.85	0.30	13	HS Fe^{II}
	0.54	0.22	0.24	87	LS Fe^{II}

[a] Isomer shift data are reported respective to iron foil. [b] Full width at half height.

Fe^{II} ($\delta = 1.11$ mm s^{-1}, $\Delta E_Q = 1.85$ mm s^{-1}) and LS Fe^{II} species ($\delta = 0.54$ mm s^{-1}, $\Delta E_Q = 0.22$ mm s^{-1}), with relative areas of 0.13 and 0.87. A deconvolution analysis of the spectra was performed to determine the HS versus total Fe^{II} molar fraction, and the results are presented in Figure 12 and Table 5. The Mössbauer spectral results are compatible with the magnetic susceptibility data.

SCO of $[Fe(H_2L^{2\text{-Me}})_2]Cl\cdot BF_4\cdot 0.6EtOH$ (2b). As shown in Figure 13, the BF_4 salt (**2b**) showed a two-step SCO behavior, which is more gradual of a transition than that of the ClO_4 salt (**2a**) and has a narrower temperature range for the intermediate spin state. A small difference between the warming and cooling modes is observed at the lower temperatures, indicative of a small frozen-in effect. Upon lowering the temperature from 350 to 5 K at a rate of 1 K min^{-1}, a $\chi_M T$ value of ca. 3.3 cm^3 K mol^{-1} in the region of 350−300 K (typical value for the HS Fe^{II} state) was measured, and the value moderately decreased from ca. 3.3 cm^3 K mol^{-1} at 300 K to 0.2 cm^3 K mol^{-1} at 5 K through the gradual intermediate plateau, where the inflection points were evaluated to be 260 and 100 K for a SCO of HS↔(HS+LS)/2 and (HS+LS)/2↔LS, respectively.

SCO of $[Fe(H_2L^{2\text{-Me}})_2]Cl\cdot PF_6\cdot 0.8EtOH$ (2c). As shown in Figure 14, the PF_6 salt (**2c**) showed a one-step SCO behavior. The magnetic behaviors in the warming and cooling modes are the same, showing neither a frozen-in effect nor hysteresis. Upon lowering the temperature from 350 to 5 K, the $\chi_M T$ value is constant at ca. 3.3 cm^3 K mol^{-1} (typical value for the HS Fe^{II} state) in the region of 350−250 K, and the value decreases from ca. 3.3 cm^3 K mol^{-1} at 250 K to 0 cm^3 K mol^{-1} (typical value for the LS Fe^{II} state) at 5 K, where the inflection point was evaluated to be 198 K for the SCO of HS ↔ LS.

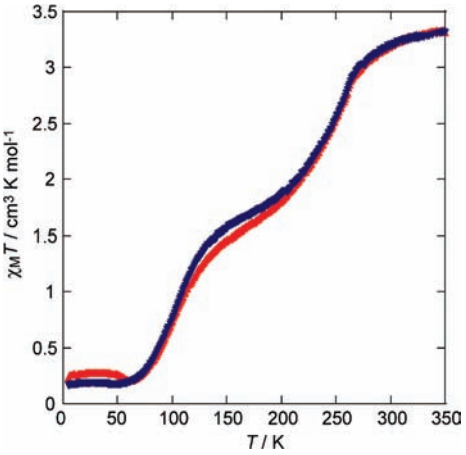

Figure 13. Magnetic behavior of $[Fe(H_2L^{2\text{-Me}})_2]Cl\cdot BF_4\cdot 0.6EtOH$ (**2b**) in the form of the $\chi_M T$ versus T plots. The sample was warmed from 5 to 350 K (red ▲) and then cooled from 350 to 5 K (blue ▼) at a sweep rate of 1 K min^{-1}.

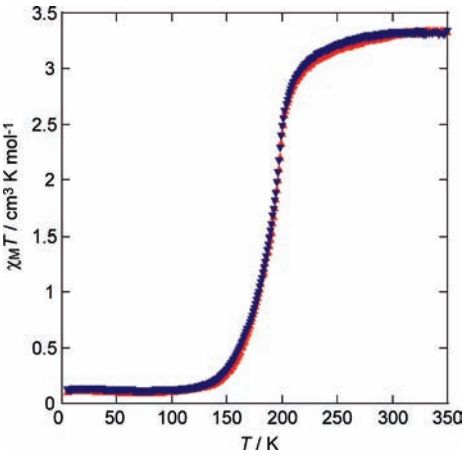

Figure 14. Magnetic behavior of $[Fe(H_2L^{2\text{-Me}})_2]Cl\cdot PF_6\cdot 0.8EtOH$ (**2c**) in the form of the $\chi_M T$ versus T plots. The sample was warmed from 5 to 350 K (red ▲) and then cooled from 350 to 5 K (blue ▼) at a sweep rate of 1 K min^{-1}.

Representative Mössbauer spectra of the solvated sample are shown in Figure 15(a). On increasing the temperature after rapid cooling to 78 K, spectra were recorded at 78, 140, 160, 180, 200, 220, 250, and 298 K. In the range 78−140 K, each spectrum consists only of a doublet attributable to the LS Fe^{II} species (for example, at 78 K, $\delta = 0.53$ mm s^{-1}, $\Delta E_Q = 0.28$ mm s^{-1}). On increasing the temperature from 140 K, the relative intensity of the doublet due to the LS state decreases, while that of the doublet due to the HS state increases, showing a one-step SCO behavior. Above 250 K, only a doublet due to the HS species is observed. A deconvolution analysis of the spectra was performed to determine the HS versus total

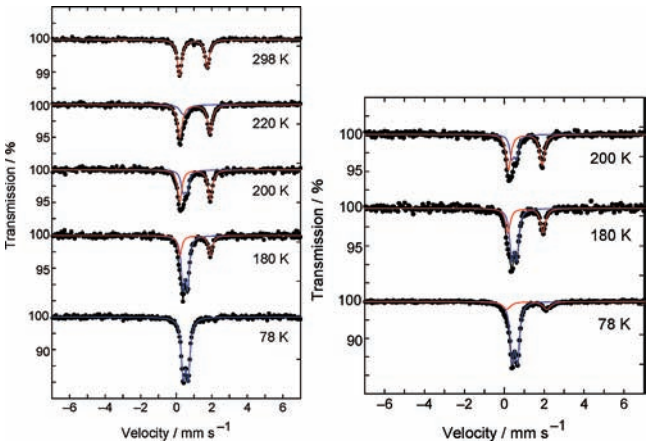

Figure 15. (a, left) Selected ^{57}Fe Mössbauer spectra of $[Fe(H_2L^{2\text{-}Me})_2]Cl\cdot PF_6\cdot 0.8EtOH$ (**2c**) recorded at 78, 180, 200, 220, and 298 K in warming mode after rapid cooling to 78 K. (b, right) Selected ^{57}Fe Mössbauer spectra of desolvated sample (**2c′**) recorded at 78, 180, and 200 K in warming mode after rapid cooling to 78 K. The HS and LS spectra generated by the deconvolution analyses are drawn in red and blue.

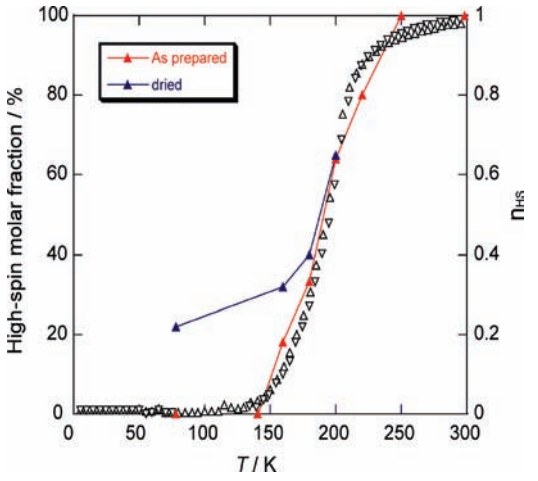

Figure 16. Molar fraction of HS versus total Fe^{II} for $[Fe(H_2L^{2\text{-}Me})_2]Cl\cdot PF_6\cdot 0.8H_2O$ (**2c**) on the solvated sample (red ▲) and desolvated sample (blue ▼) obtained by deconvolution analysis of the Mössbauer spectra, together with the molar fraction n_{HS} obtained from the magnetic susceptibility measurements. n_{HS} was calculated by using the equation $(\chi_M T)_{obs}=n_{HS}(\chi_M T)_{HS}+(1-n_{HS})(\chi_M T)_{LS}$, with $(\chi_M T)_{HS}=3.5\ cm^3\ K\ mol^{-1}$ and $(\chi_M T)_{LS}=0.0\ cm^3\ K\ mol^{-1}$ as limiting values.

Fe^{II} molar fraction and the results are presented in Figure 16 and Table 6. The Mössbauer and magnetic susceptibility results are almost consistent. In addition, to examine the effect of solvent molecules on the SCO, the desolvated sample **2c'** was prepared by drying **2c**. Representative Mössbauer spectra of the desolvated sample are shown in Figure 15(b). On increasing the temperature of the desolvated sample after rapid cooling to 78 K, spectra were recorded at 78, 160, 180, and 200 K. At 78 K, the spectrum consists of two doublets attributable to the HS Fe^{II} ($\delta=1.13$ mm s^{-1}, $\Delta E_Q=2.01$ mm s^{-1}) and LS Fe^{II} species ($\delta=0.53$ mm s^{-1}, $\Delta E_Q=0.28$ mm s^{-1}), with relative areas of 0.22 and 0.78. The area ratio of HS state is larger than that of the solvated sample. This result suggests that the crystal solvent affects on SCO properties for the compound $[Fe(H_2L)_2]Cl\cdot PF_6\cdot 0.8$ EtOH (**2c**).

Table 6. Mössbauer Parameters for $[Fe(H_2L^{2\text{-}Me})_2]Cl\cdot PF_6\cdot 0.8H_2O$ (**2c**)

On Heating after Rapid Cooling down to 78 K					
temp/K	δ^a/mm s^{-1}	ΔE_Q/mm s^{-1}	Γ^b/mm s^{-1}	area ratio/%	assignment
298	0.97	1.56	0.30	100	HS Fe^{II}
250	1.03	1.62	0.33	100	HS Fe^{II}
220	1.05	1.69	0.31	80	HS Fe^{II}
	0.45	0.22	0.40	20	LS Fe^{II}
200	1.05	1.72	0.29	64	HS Fe^{II}
	0.49	0.23	0.27	36	LS Fe^{II}
180	1.06	1.72	0.27	33	HS Fe^{II}
	0.50	0.26	0.23	67	LS Fe^{II}
160	1.07	1.76	0.30	18	HS Fe^{II}
	0.52	0.26	0.24	82	LS Fe^{II}
140	0.51	0.27	0.25	100	LS Fe^{II}
78	0.53	0.28	0.26	100	LS Fe^{II}
On Heating after Rapid Cooling down to 78 K (Desolvated Sample)					
temp/K	δ^a/mm s^{-1}	ΔE_Q/mm s^{-1}	Γ^b/mm s^{-1}	area ratio/%	assignment
200	1.05	1.69	0.29	65	HS Fe^{II}
	0.49	0.23	0.24	35	LS Fe^{II}
180	1.06	1.76	0.29	40	HS Fe^{II}
	0.50	0.26	0.24	60	LS Fe^{II}
160	1.07	1.85	0.36	32	HS Fe^{II}
	0.51	0.26	0.23	68	LS Fe^{II}
78	1.13	2.01	0.47	22	HS Fe^{II}
	0.53	0.28	0.26	78	LS Fe^{II}

[a] Isomer shift data are reported relative to iron foil. [b] Full width at half height.

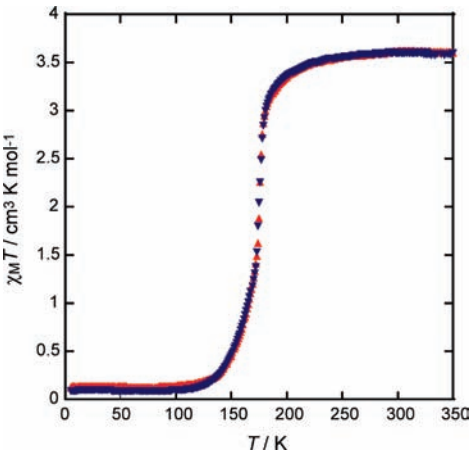

Figure 17. Magnetic behavior of $[Fe(H_2L^{2\text{-}Me})_2]Cl\cdot AsF_6\cdot 0.9EtOH$ (**2d**) in the form of $\chi_M T$ versus T plots. The magnetic data were measured in the warming mode from 5 to 350 K (red ▲) and then cooling mode from 350 to 5 K (blue ▼) at a sweep rate of 1 K min^{-1}.

SCO of $[Fe(H_2L^{2\text{-}Me})_2]Cl\cdot AsF_6\cdot 0.9EtOH$ (2d). As shown in Figure 17, the SCO behavior of the AsF_6 salt (**2d**) showed a steep one-step SCO behavior and no frozen-in effect. It should be noted that the inflection points evaluated for SCO behaviors in the warming and cooling modes were slightly different, suggesting a small thermal hysteresis. The evaluated inflection points $T_{1/2\uparrow}$ and $T_{1/2\downarrow}$ were 175 and 173 K, respectively. This result indicates the occurrence of a ca. 2 K width thermal hysteresis. Upon lowering the temperature from 350 to 5 K at a rate of 1 K min^{-1}, a $\chi_M T$ value of ca. 3.6 cm^3 K mol^{-1} in the region of 350−200 K (typical value for HS Fe^{II} state) was measured, and the value abruptly decreased

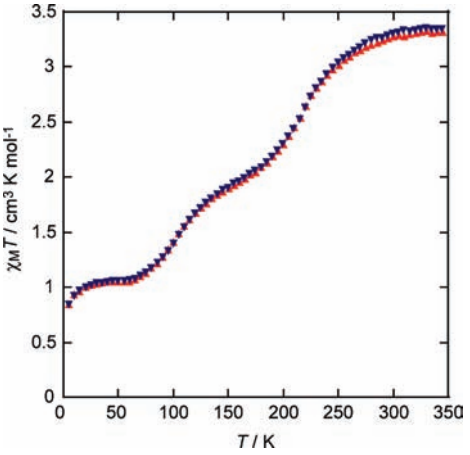

Figure 18. A gradual and incomplete two-step SCO behavior of **2a′** in the form of $\chi_M T$ versus T plots. The magnetic data were measured in the warming mode from 5 to 350 K (red ▲) and then cooling mode from 350 to 5 K (blue ▼) at a sweep rate of 1 K min^{-1}.

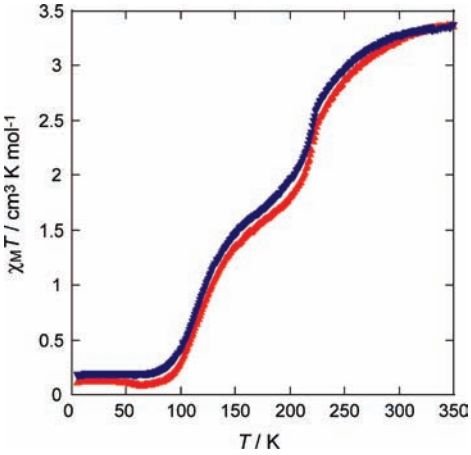

Figure 19. Two-step SCO behaviors of **2a″** in the form of $\chi_M T$ versus T plots. The magnetic data were measured in the warming mode from 5 to 350 K (red ▲) and then cooling mode from 350 to 5 K (blue ▼) at a sweep rate of 1 K min^{-1}.

from ca. 3.6 cm^3 K mol^{-1} at 200 K to 1.5 cm^3 K mol^{-1} (a value for the (HS+LS)/2 Fe^{II} state) at 170 K, thereafter less abruptly decreased to ca. 0 cm^3 K mol^{-1} (typical value for the LS Fe^{II} state) at 5 K.

SCO of $[Fe(H_2L^{2\text{-}Me})_2]Cl\cdot ClO_4\cdot 0.5(1\text{-}PrOH)\cdot 1.5H_2O$ (2a′). As shown in Figure 18, $[Fe(H_2L^{2\text{-}Me})_2]Cl\cdot ClO_4\cdot 0.5(1\text{-}PrOH)\cdot 1.5H_2O$ (**2a′**) showed a gradual incomplete two-step SCO, where the inflection points were evaluated to be 220 and 100 K. These two temperatures are compared with those of **2a**, $T_{1/2,2}=255$ and $T_{1/2,1}=75$ K. The $\delta T=110$ K of **2a′** is smaller than the $\delta T=180$ K of **2a**.

SCO of $[Fe(H_2L^{2\text{-}Me})_2]Br\cdot ClO_4\cdot 0.5EtOH$ (2a″). As shown in Figure 19, the $NH\cdots Br^-$ bridged complex (**2a″**) showed a rather gradual two-step SCO, where the inflection points were evaluated to be 220 and 110 K. The magnetic behaviors in the warming and cooling modes show a difference in the steepness of SCO, where the second run in the cooling mode from 350 to 5 K gives a more gradual SCO than the first run. The first transition temperature was lower than that of **2a**, while the second one was higher than that of **2a**.

Structures of $[Fe(H_2L^{2\text{-}Me})_2]Br\cdot ClO_4\cdot EtOH$ (2a″) in the HS, Intermediate of (HS+LS)/2, and LS States. The crystal structure of **2a″** was determined by single-crystal X-ray diffraction analysis at 296, 175, and 103 K, in order to investigate the structures in the HS, intermediate (HS+LS)/2, and LS states. Table 7 shows the crystallographic data at three temperatures, showing that the cell dimensions at the three temperatures are similar to each other, but the crystal system changes from a monoclinic system in the HS state to a triclinic system in the intermediate and LS states. The monoclinic space group $P2_1/n$ at 296 K converts to the triclinic space group $P\bar{1}$ at 175 and 103 K. Thus, the HS state consists of a single iron(II) crystallographic site, and the intermediate state consists of two iron(II) crystallographic sites. In addition to the deformation of the unit cell during the SCO process from the HS to LS state through (HS + LS)/2, the dimensions of a and c are shortened, but that of b is elongated. It should be noted that the $\alpha=92.0°$ and $\gamma=88.1°$ angles of the triclinic system in the intermediate state at 175 K are much more deviated from 90° than the corresponding angles ($\alpha=89.2°$ and $\gamma=90.8°$) in the LS state at 103 K. So if a lower temperature than 103 K was set to reach the perfect LS state, the monoclinic system might be obtained. The sequence of three phases may be described as "re-entrant" in the sense that the unit cell of the HS structure seems to reappear in the LS structure but differs from that in the intermediate state, as observed in $[Fe(2\text{-pic})_3]Cl_2\cdot EtOH$ (2-pic = picolylamine).[12a]

The same cell-axis setting, that is, not the standard setting for a triclinic system, is taken throughout the structures at three temperatures so as to investigate the structural change easily during the spin transition. The cell volume changes from 2935(2) $Å^3$ at 296 K to 2880(3) $Å^3$ at 175 K, and to 2845(2) $Å^3$, showing 1.9% and 1.2% volume reductions for HS → (HS+LS)/2 and (HS+LS)/2 → LS, respectively. The volume reduction of **2a″** is much smaller than those of **2c**, **2d**, and the other SCO complexes, probably due to **2a″** accompanying a change of crystal system. Table 8 gives the selected bond distances and hydrogen-bond distances. The coordination angles are given in Supporting Information S3.

Complex **2a″** in the HS state at 296 K has an isomorphous structure to **2a**−**2d** and consists of one molecular unit. The Fe−N bond distances (2.11−2.16 Å) are in the range for the HS Fe^{II} complex with similar N_6 donor atoms. Compound **2a″** in the intermediate state of (HS + LS)/2 at 175 K and the LS state at 103 K consists of two molecular units. At 175 K, two independent Fe^{II} sites, Fe(1) and Fe(2), assume Fe(1)−N bond distances of 1.96−2.01 Å and Fe(2)−N bond distances of 2.08−2.16 Å, which are the distances expected for the LS and HS Fe^{II} complexes, respectively. The N−Fe−N bond angles also indicate that Fe(1) assumes the LS state and Fe(2) assumes the HS state, since the value around Fe(1) is closer to a regular octahedron than that of Fe(2). At 103 K, the Fe(1)−N bond distances of 1.99−2.03 Å and Fe(2)−N bond distances of 1.98−2.04 Å are the typical distances expected for the LS Fe^{II} complex.

(12) (a) Chernyshov, D.; Hostettler, M.; Törnroos, K. W.; Bürgi, H.-B. *Angew. Chem., Int. Ed.* **2003**, *42*, 3825–3830. (b) Sorai, M.; Nakano, M.; Miyazaki, Y. *Chem. Rev.* **2006**, *106*, 976–1031.

Table 7. Crystallographic Data of **2a**″ in the HS (296 K), Intermediate (HS + LS)/2 (175 K), and LS States (103 K)

complex	296 K	175 K	103 K
formula	$C_{22}H_{32}N_{10}BrClO_5Fe$	$C_{22}H_{32}N_{10}BrClO_5Fe$	$C_{22}H_{32}N_{10}BrClO_5Fe$
fw	687.76	687.76	687.76
space group	$P2_1/n$ (No. 14)	$P\bar{1}$ (No. 2)	$P\bar{1}$ (No. 2)
a, Å	11.972(5)	11.870(5)	11.868(5)
b, Å	19.065(10)	19.171(9)	19.150(9)
c, Å	12.897(6)	12.712(8)	12.564(7)
α deg	90	92.06(2)	89.23(2)
β, deg	94.357(15)	94.79(2)	94.85(2)
γ, deg	90	88.11(2)	90.87(2)
V, Å^3	2935(2)	2880(3)	2845(2)
Z	4	4	4
T, K	296	175	103
D_{calcd}, g cm^{-3}	1.556	1.586	1.606
R, R_w[a]	0.0414, 0.0580	0.1588, 0.1870	0.1459, 0.1742

Table 8. Relevant Coordination Bond Lengths (Å) and Hydrogen Bond Lengths (Å) for **2a**″ at 296, 175, and 103 K

complex	**2a**″ (296 K)	**2a**′ (175 K)	**2a**″ (103 K)
Fe(1)−N(2), Fe(2)−N(12)	2.118(14)	1.965(12), 2.125(12)	2.028(15), 1.997(14)
Fe(1)−N(3), Fe(2)−N(13)	2.149(13)	1.987(13), 2.130(14)	2.030(16), 1.982(15)
Fe(1)−N(5), Fe(2)−N(15)	2.111(15)	2.011(11), 2.119(13)	2.021(14), 2.039(14)
Fe(1)−N(7), Fe(2)−N(17)	2.123(14)	2.013(13), 2.159(13)	2.005(15), 2.004(15)
Fe(1)−N(8), Fe(2)−N(18)	2.161(11)	1.985(13), 2.160(13)	2.027(15), 2.000(17)
Fe(1)−N(10), Fe(2)−N(20)	2.128(11)	1.990(13), 2.081(14)	1.988(15), 2.008(15)
	Br(1)···O(5), 3.427(12)	Br(1)···N(9), 3.318(16)	Br(1)···O(9), 3.369(19)
	Br(1)···N(1), 3.39(2)	Br(1)···N(16), 3.519(15)	Br(1)···N(1), 3.237(17)
	Br(1)···N(4), 3.420(15)	Br(2)···O(10), 3.365(17)	Br(1)···N(9), 3.413(18)
	Br(1)···N(6), 3.318(13)	Br(2)···N(6), 3.320(15)	Br(1)···N(16), 3.349(18)
		Br(2)···N(11), 3.279(15)	Br(2)···N(6), 3.51(2)
		Br(2)···N(19), 3.449(15)	Br(2)···N(11), 3.328(14)
			Br(2)···N(19), 3.311(19)

Figure 20a and b show the superimposed structures of HS−(HS+LS)/2 and (HS+LS)/2−LS, respectively, showing the unit cell deformation and structural change in a unit cell during the two-step spin transition. The molecular volume change of the Fe^{II} species due to the spin transition brings the deformation of the intermolecular network structure, evidenced by the NH···Br^- hydrogen-bond distances. In the HS and LS states, a similar network structure is observed. In the intermediate spin state of (HS+LS)/2, where the HS and LS species with different molecular volumes coexist in the crystal lattice, the deformation of the network structure is extraordinary large in the present system and accompanies the formation of a new network structure, a deformation of the unit cell, and a change of the crystal system and space group. Figure 21a−c show the crystal structures in the HS, (HS+LS)/2, and LS states, respectively, where the crystal packing diagrams projected along the *a* axis together with the unit cell are drawn, and the HS and LS Fe^{II}

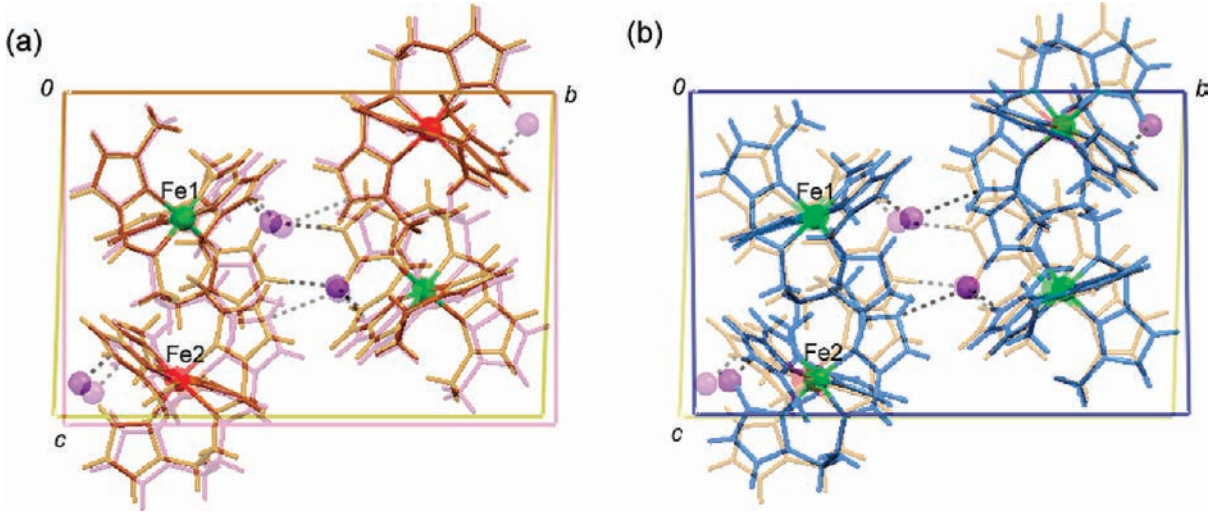

Figure 20. (a) Superimposed structure of (HS + LS)/2 on that of the HS state of **2a**″ projected on the *bc* plane. (b) Superimposed structure of LS on that of (HS + LS)/2 of **2a**″ projected on the *bc* plane. The figures show the unit cell deformation and structural change in a unit cell during the two-step spin transition. The HS, (HS+LS)/2, and LS molecules are drawn in red-violet, yellow-brown, and blue, respectively. The HS and LS Fe^{II} ions are drawn as red and green balls, respectively.

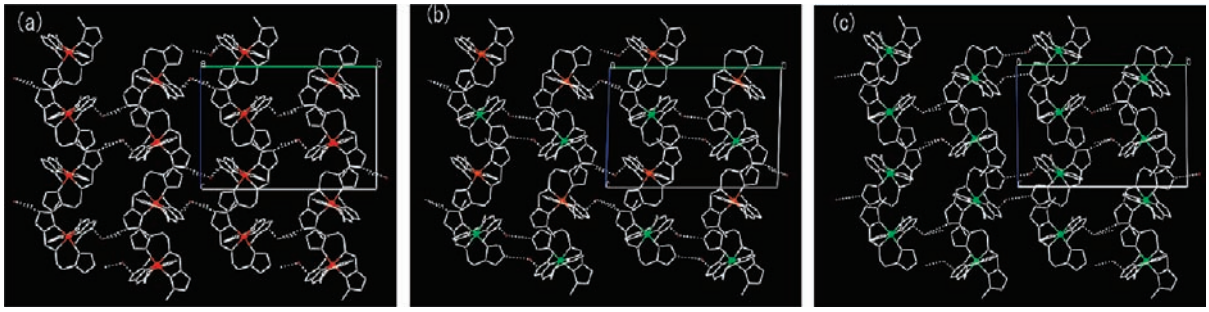

Figure 21. Hydrogen-bonded 2D network structure of $[Fe(H_2L^{2\text{-}Me})_2]Br\cdot ClO_4\cdot EtOH$ (**2a**′′) in the HS, (HS + LS)/2, and LS states, where the anions ClO_4^- and EtOH are omitted for clarity, and HS and LS iron(II) ions are drawn in red and green, respectively. (a) Network structure in the HS state at 296 K projected along the *a* axis. (b) Network structure in the state of (HS + LS)/2 at 175 K projected along the *a* axis. (c) Network structure in the LS state at 103 K projected along the *a* axis.

ions are drawn in red and green, respectively. In the intermediate state, the layer of HS molecules and the layer of LS molecules are alternately arrayed to give a long-range ordering. According to the literarure,[13] the occurrence of a largely ordered intermediate state implies that long-range correlations of HS and LS complexes are energetically more favorable than the short-range correlations. In the intermediate spin state (see Figure 21b), the layer of HS molecules as well as that of LS molecules involves two enantiomorphs. Two enantiomorphs are connected by the hydrogen bonds to form a dinuclear structural unit.

Effects of the Size of the Anion, Crystal Solvents, and Halogen Ion on the SCO of 2D Complexes. The abrupt and two-step SCO properties observed for **1**, **1**′, and **2a**−**2d** come from the cooperativity resulting from the network structure constructed by the NH···Cl^- hydrogen bonds. The effects of the size of the anion, crystal solvents, and halogen ion on the SCO properties were examined. Since **2a**−**2d**, **2a**′, and **2a**′′ assume an isomorphous structure of a 2D network constructed by the NH···Cl^- (or Br^-) hydrogen bonds between the SCO sites, it is possible to make a correlation between the SCO properties and structural parameters. At first, we will consider the effect of the anion size on the SCO. Figure 22 shows the $\chi_M T$ versus T plots of $[Fe(H_2L^{2\text{-}Me})_2]Cl\cdot X\cdot n$EtOH, **2a**−**2d** (X = ClO_4, BF_4, PF_6, and AsF_6), in the cooling mode from 350 to 5 K, representing a variety of SCO properties depending on the counteranion X. The counteranions used in this study can be described as isotropic molecules, and the molecular volumes evaluated by quantum-chemical calculations are 53.4 Å for BF_4^-, 54.4 Å for ClO_4^-, 73.0 Å for PF_6^-, and 78.5 Å for AsF_6^-.[14] The ClO_4^- (**2a**) and BF_4^- (**2b**) salts with smaller volume anions showed a two-step SCO of HS ↔ (HS + LS)/2 ↔ LS, while the PF_6 (**2c**) and AsF_6 (**2d**) salts with larger volume anions showed a one-step SCO of HS ↔ LS. As the size of the anion becomes large, the SCO begins to move from two-step to one-step behavior. This tendency of the size of the anion on the SCO property is in accord with our previous SCO complexes of $[Fe(H_3L^{Me})]Cl\cdot X$ (X = PF_6^-, AsF_6^-, SbF_6^-; H_3L^{Me} = tris[2-{[(2-methylimidazol-4-yl)methylidene]amino}ethyl]amine),[10a] in which the complexes have an isomorphous 2D network

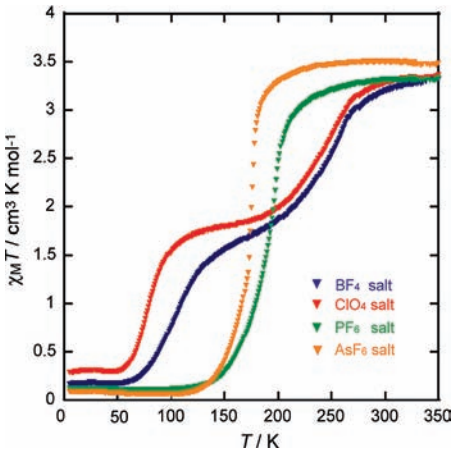

Figure 22. Anion size effect on 2D SCO complexes $[Fe(H_2L^{2\text{-}Me})_2]Cl\cdot X\cdot EtOH$ (X=ClO_4 (**2a**), BF_4 (**2b**), PF_6 (**2c**), and AsF_6 (**2d**)). The plots of $\chi_M T$ vs T in the cooling modes at a 1 K min^{-1} sweep rate are shown; the ClO_4^- salt (red ▼), BF_4^- salt (blue ▼), PF_6^- salt (green ▼), and AsF_6^- salt (orange ▼).

structure constructed by NH···Cl^- hydrogen bonds and the anion X is just accommodated in the space between the 2D layers. There are structural differences between the two groups (two-step SCO, **2a** and **2b**; one-step SCO, **2c** and **2d**) in the dimensions of three NH···Cl^- hydrogen bonds. As given in Table 4, the distance of N(6)···Cl is the shortest distance of three NH···Cl^-'s, ca. 3.1 Å for the four complexes. In one-step SCO complexes **2c** and 2d, the distances of N(1)···Cl and N(4)···Cl are long, ca. 3.35 Å in the HS state, while the distance of N(4)···Cl becomes short, ca. 3.2 Å, and that of N(1)···Cl shows no change in the LS state. Considering two closer hydrogen bonds, N(6)···Cl and N(4)···Cl, **2c** and **2d** can be described as a binuclear structural unit, in which two opposite enantiomorphs are hydrogen-bonded through two Cl^- ions. On the other hand, these two distances in two-step SCO complexes **2a** and **2b** are rather close to that of N(6)···Cl. The closer three hydrogen bonds observed for **2a** and **2b** must be the structural parameters for two-step SCO, because the strong cooperative 2D structure is constructed by the three short NH···Cl^- hydrogen bonds. Although the anion X itself is not involved in the 2D network, the volume of the anion affects indirectly the 2D network, weakening some of the hydrogen bonds, when the molecular volume of the Fe^{II} species changes during the spin transition.

(13) (a) Romstedt, H.; Spiering, H.; Gütlich, P. *J. Phys. Chem. Solids* **1998**, *59*, 1353. (b) Spiering, H.; Kohlhaas, T.; Romstedt, H.; Hauser, A.; Brun-Yilmaz, C.; Kusz, J.; Gutlich, P. *Coord. Chem. Rev.* **1999**, *190*−*192*, 629.
(14) *Spartan*, version 4.0, Wavefunction, Inc.: Irvine, CA, 1999.

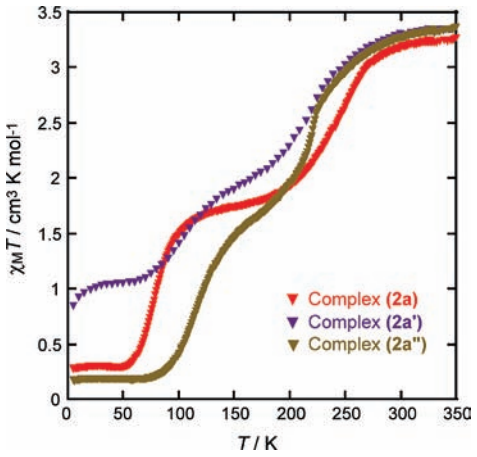

Figure 23. Crystal solvent and bridging halogen ion effects on 2D SCO complexes. The plots of $\chi_M T$ vs T in the cooling modes for $[Fe(H_2L^{2\text{-}Me})_2]Cl\cdot ClO_4\cdot 0.5EtOH$ (**2a**; red ▼), $[Fe(H_2L^{2\text{-}Me})_2]Cl\cdot ClO_4\cdot 0.5(1\text{-}PrOH)\cdot 1.5H_2O$ (**2a′**; purple ▼), and $[Fe(H_2L^{2\text{-}Me})_2]Br\cdot ClO_4\cdot 0.5EtOH$ (**2a″**; brown ▼).

Figure 23 shows the $\chi_M T$ versus T plots of $[Fe(H_2L^{2\text{-}Me})_2]Cl\cdot ClO_4\cdot 0.5EtOH$ (**2a**), $[Fe(H_2L^{2\text{-}Me})_2]Cl\cdot ClO_4\cdot 0.5(1\text{-}PrOH)\cdot 1.5H_2O$ (**2a′**), and $[Fe(H_2L^{2\text{-}Me})_2]Br\cdot ClO_4\cdot 0.5EtOH$ (**2a″**) in the cooling mode, representing the effect of the crystal solvent and bridging halogen ion. $[Fe(H_2L^{2\text{-}Me})_2]Cl\cdot ClO_4\cdot 0.5(1\text{-}PrOH)\cdot 1.5H_2O$ (**2a′**) showed a gradual incomplete two-step SCO, where the inflection points were evaluated to be 220 and 100 K. Since the chemical formulas obtained from the X-ray analysis and the magnetic measurements are different, the discussion should be limited to the primary level. Nevertheless, it is apparent that two of three NH···Cl^- hydrogen bonds are elongated, compared with those of **2a**, due to the larger crystal solvent and additional water molecule. The gradual incomplete two-step SCO of **2a′** can be rationalized by the disappearance of the multidimensional hydrogen bond. The NH···Br^- bridged complex (**2a″**) showed a rather gradual two-step SCO compared to that of the corresponding NH···Cl^- complex (**2a**), where the inflection points of **2a″** shifted to lower and higher values. The gradual two-step SCO might be brought about by elongation of the hydrogen bonds NH···Cl^- or three long NH···Br^- bonds, where the volume reduction or expansion of the SCO species due to the spin transition is not effectively transmitted over the crystal lattice.

Two-Step SCO of the Present and Reported Complexes. Regarding the two-step SCO, it should be valuable that a comparison of the present compounds is made to the reported Fe(II) mononuclear, dinuclear, and polymeric compounds. According to the investigation on the crystal structures of SCO complexes, Sorai et al.[12b] pointed out that the phase transition without change in the space group seems to be characteristic of SCO phenomena. However, this is not the case for the two-step SCO complexes, as he also noted. The most fully investigated mononuclear complexes displaying two-step SCO can be $[Fe(2\text{-}pic)_3]Cl_2\cdot C_2H_5OH$.[12] Sorai et al.[12b] observed two peaks at 114.0 and 122.2 K at a molar heat capacity corresponding to the two-step spin conversion. On the basis of a single-crystal X-ray study, Bürgi et al. showed that the structure undergoes two first-order phase transitions, where the space groups are $B2_1/c$ in the HS and LS phases and $P2_1/c$ in the intermediate phase.[12a] We have reported a two-step SCO of $[FeH_3L^{Me}]Cl\cdot X$ (H_3L^{Me} = tris[2-{[(2-methylimidazol-4-yl)methylidene]amino}ethyl]-amine, X = PF_6, AsF_6), in which the space group changes from $P2_1/n$ in the HS state, through $P2_1$ in the intermediate spin state, to $P2_1/n$ in the LS state.[10a] [Fe{5-NO_2-sal-N(1,4,7,10)}] is the first two-step SCO complex, in which the space group changes between the LS phase, the mixed intermediate phase, and the HS phase.[15a] Matouzenko et al. reported the two-step SCO in [Fe(Hpy−DAPP)]-$(BF_4)_2$ (Hpy-DAPP = {bis[N-(2-pyridylmethyl)-3-amino-propyl](2-pyridylmethyl)amine}), where the space group does not change and the complex gives the first example presenting a single iron(II) crystallographic site in the whole temperature range. The two-step SCO is induced by two different geometries of the $[FeN_6]$ coordination core generated in the lattice by the disorder in the ligand.[15b] The complex $[Fe(picpzpz)_2](BF_4)_2\cdot MeOH$ (pipzpz = 2-(1-pyridin-2-ylmethyl-1H-pyrazol-3-yl)pyrazine) displays a two-step spin transition with a gradual higher-temperature step ($T_{1/2}$ = 197 K) and an abrupt low-temperature step with hysteresis ($T_{1/2}$ = 91/98 K). The single-crystal X-ray diffraction analyses showed the unit cell parameter evolution versus temperature, while they showed no change of space group.[15c] Some dinuclear complexes exhibit a two-step SCO phenomenon, [LS−LS] ↔ "[LS−HS]" ↔ [HS−HS]. Murray and co-workers confirmed for the first time the existence of the mixed spin state [LS−HS] from X-ray crystallographic data of the doubly 1,2,4-triazole-bridged complex $[Fe_2(PMAT)_2](BF_4)_4\cdot DMF$, in which the unit cell doubles in the [HS−LS] state.[15d] Kojima et al. reported a binuclear SCO complex of bis(imidazolylimine) ligand $[Fe_2(H_2L^H)_3](ClO_4)_4$ exhibiting "[LS-HS]" ↔ [HS−HS], in which the spin conversion is associated with the presence of two different iron(II)'s without a change of the space group.[15e] Some polymeric complexes are known to exhibit a two-step SCO. In the case of $[Fe(btr)_3](ClO_4)_2$ (btr = 4,4′-bis-1,2,4-triazole), Garcia et al. reported that the two-step spin conversion is associated with the presence of two slightly different iron(II) sites, whereas the space group (trigonal $R\bar{3}$) remains identical independently of the spin state.[15f] In the case of $Fe(bpe)_2(NCS)_2\cdot 3$acetone (bpe = 1,2-bis(4′-pyridyl)ethane, the compound displays a two-step SCO in a nanoporous metal−organic framework, accompanying the change of the crystal system and space group.[15g] Due to the limited number of two-step SCO complexes, the discussion should be limited. However, one can say that two-step SCO mostly accompanies the change in the space group, and at least the intermediate state is the expression of a structure with two different iron sites showing long-range order.

(15) (a) Boinnard, D.; Bousseksou, A.; Dworkin, A.; Savariault, J. M.; Varret; Tuchagues, J. P. *Inorg. Chem.* **1994**, *33*, 271. (b) Matouzenko, G. S.; Luneau, D.; Molnár, G.; Ould-Moussa, N.; Zein, S.; Borshch, S. A.; Bousseksou, A.; Averseng, F. *Eur. J. Inorg. Chem.* **2006**, 2671–2682. (c) Leita, B. A.; Neville, S. M.; Halder, G. J.; Moubaraki, B.; Kepert, C. J.; Letard, J. F.; Murray, K. S. *Inorg. Chem.* **2007**, *46*, 8784–8795. (d) Klingele, M. H.; Moubaraki, B.; Cashion, J. D.; Murray, K. S.; Brooker, S. *Chem. Commun.* **2005**, 987–989. (e) Fujita, K.; Kawamoto, R.; Tsubouchi, R.; Sunatsuki, Y.; Kojima, M.; Iijima, S.; Matsumoto, N. *Chem. Lett.* **2007**, *36*, 1284–1285. (f) Garcia, Y.; Kahn, O.; Rabardel, L.; Chansou, B.; Salmon, L.; Tchagues, J. P. *Inorg. Chem.* **1999**, *38*, 4663–4670. (g) Halder, G. J.; Chapman, K. W.; Neville, S. M.; Moubaraki, B.; Murray, K. S.; Letrad, J. F.; Kepert, C. J. *J. Am. Chem. Soc.* **2008**, *130*, 17552–17562.

Table 9. The First and Second SCO Transition Temperatures ($T_{1/2,1}$ and $T_{1/2,2}$) and the Width δT Defined by $\delta T = T_{1/2,2} - T_{1/2,1}$[a]

complex	$T_{1/2,1}$	$T_{1/2,2}$	δT	
$[Fe(H_2L^{2\text{-Me}})_2]Cl\cdot ClO_4\cdot 0.5EtOH$ (**2a**)	75	255	180	mononuclear
$[Fe(H_2L^{2\text{-Me}})_2]Cl\cdot BF_4\cdot 0.6EtOH$ (**2b**)	100	260	160	mononuclear
$[Fe(H_2L^{2\text{-Me}})_2]Cl\cdot PF_6\cdot 0.8EtOH$ (**2c**)	198		0	mononuclear, no space group change
$[Fe(H_2L^{2\text{-Me}})_2]Cl\cdot AsF_6\cdot 0.9EtOH$ (**2d**)	175		0	mononuclear, no space group change
$[Fe(H_2L^{2\text{-Me}})_2]Cl\cdot ClO_4\cdot 0.5(1\text{-PrOH})\cdot 1.5H_2O$ (**2a′**)	100	220	120	mononuclear
$[Fe(H_2L^{2\text{-Me}})_2]Br\cdot ClO_4\cdot 0.5EtOH$ (**2a″**)	110	220	110	mononuclear, space group change
$[Fe(2\text{-pic})_3]Cl_2\cdot C_2H_5OH$[12a]	114	122	8	mononuclear, space group change
$[FeH_3L^{Me}]Cl\cdot AsF_6$[10a]	85	120	35	mononuclear
$[Fe(picpzpz)_2](BF_4)\cdot 2MeOH$[15c]	98 or 91	197	99	mononuclear
$Fe(bpe)_2(NCS)_2\cdot 3(acetone)$[15b]	80	133	53	polynuclear
$[Fe(btr)_3](ClO_4)_2$[15e]	184	222	38	polynuclear

[a] 2-pic=picolylamine, H_3L^{Me}=tris[2-{[(2-methylimidazol-4-yl)methylidene]amino}ethyl]amine, picpzpz=2-(1-pyridin-2-ylmethyl-1H-pyrazol-3-yl)-pyrazine, bpe=1,2-bis(4′-pyridyl)ethane, btr=4,4′-bis-1,2,4-triazole.

At this stage, the experimental results, especially two-step SCO behaviors, are examined on the basis of the structures. Table 9 lists the data of $T_{1/2,1}$, $T_{1/2,2}$, and δT (= $T_{1/2,2}-T_{1/2,1}$) for the present series of SCO complexes as well as those of the SCO complexes in the literature,[10a,15] where $T_{1/2,1}$ and $T_{1/2,2}$ are the SCO transition temperatures of LS ↔ (HS + LS)/2 and (HS + LS)/2 ↔ HS, respectively, and they were evaluated by the maximum of $\delta(\chi_M T)/\delta T$. As given in Table 9, **2a**, **2b**, **2a′**, and **2a″** show a two-step behavior, while **2c** and **2d** show a one-step behavior. The δT value of **2a** is one of the largest values reported so far. On the other hand, the δT values of **2c** and **2d** are practically zero due to one-step SCO. A drastic difference between complexes **2a** and **2b** and complexes **2c** and **2d** must be hidden in relation to their structures within the same framework of the 2D network. As noted above, even in their HS states, there are structural differences between the two groups, complexes **2a** and **2b** and complexes **2c** and **2d**, in the dimensions of three NH···Cl^- hydrogen bonds. One-step SCO complexes **2c** and **2d** can rather be described as a binuclear complex, in which two opposite enantiomorphs in a binuclear unit are hydrogen-bonded through two Cl^- ions, and the binuclear units are weakly linked. On the other hand, three closer NH···Cl^- hydrogen bonds in two-step SCO complexes **2a** and **2b** give the 2D structure definitively, and the resulting long-range cooperativity must be the structural parameters for two-step SCO.

It was confirmed experimentally that, during the spin transition, **2c** and **2d** showed no change in the crystal lattice and space group, whereas **2a** (preliminary X-ray data in the intermediate state) and **2a″** changed from a monoclinic system in the HS state to a triclinic system in the intermediate spin state of (HS + LS)/2. The molecular volume reduction of the Fe^{II} species from a HS to LS transition would bring a deformation of the intermolecular network structure in the crystal lattice, because the HS and LS species have different molecular volumes. In the intermediate spin state of (HS+LS)/2, where the HS and LS species with different molecular volumes coexist in the crystal lattice, it is anticipated that the deformation of the network structure is extraordinary large and anisotropic. Although anion X^- and EtOH themselves are not involved in the network, they affect indirectly to the deformation of the network by the occupation of their molecular volumes when the spin transition occurred. The present result of **2a** revealed that the molecular volumes of ClO_4^-−EtOH would adapt a stable network structure in the intermediate state, accompanying the change of crystal system from monoclinic to triclinic. On the other hand, on the basis of the one-step SCO of **2c** and **2d**, PF_6^-−EtOH and AsF_6^-−EtOH seem to be too large to accept a change of crystal system and give a stable network structure for the intermediate state. In this study, three complexes, **2c**, **2d**, and **2a″**, are subjected to X-ray analyses in both the HS and LS states. As given in Table 3, the *a*, *b*, and *c* unit cell parameters of **2c** and **2d** decrease in dimensions during the one-step SCO from the HS to LS state, in which *b* decreases the most. On the other hand, for a two-step SCO complex, **2a″**, as given in Table 7, *a* and *c* are shortened but *b* is elongated in comparison with the cell dimensions in the HS and LS states.

Correlation between Experimental Results and the Theoretical Model. In order to take into account the cooperativity in the SCO transition, Ising-like models first proposed by Wajnflasz and Pick have been widely used for the description of the SCO transition.[7] The two-step SCO transitions were modeled by introducing antiferromagnetic-like coupling, J_{AB}, where the interaction between the sublattices favoring the opposite configuration (HS−LS) can give two-step SCO.[7] According to the theoretical model calculation by Nishino et al. using a two-sublattice Ising-like Hamiltonian,[7] the width δT of the plateau of (HS + LS)/2 is given by $\delta T = 4z_{AB}J_{AB}/k_B \ln g$. So the δT depends only on antiferromagnetic-like coupling J_{AB}. There are structural differences between the two groups (two-step SCO, **2a** and **2b**; one-step SCO, **2c** and **2d**) in the dimensions of three NH···Cl^- hydrogen bonds, where J_{AB} must be zero for one-step SCO complexes **2c** and **2d**. The distance of N(6)···Cl is the shortest distance, ca. 3.1 Å for the four complexes. On the other hand, the distances of N(1)···Cl and N(4)···Cl are elongated in one-step SCO complexes **2c** and **2d**, but these are rather close to that of N(6)···Cl in two-step SCO complexes **2a** and **2b**. These data demonstrate that the closer multicontacts of NH···Cl^- hydrogen bonds observed in **2a** and **2b** must be the structural parameters for two-step SCO and the strong cooperativity; that is, the large J_{AB} value must be related to the multiple and shorter hydrogen bonds. However, it is difficult to see the precise relation between the distinct structural parameter and antiferromagnetic-like coupling J_{AB}. As shown in Figure 21b, in the intermediate state, the

layer of HS molecules and the layer of LS molecules are alternately arrayed, and this ordering might be related to J_{AB}.

Whether the spin transition can be of the first order (discontinuous) or gradual (continuous) depends on the value of the ferromagnetic intrasublattice interaction J of the Ising-like model. With an increase in J that corresponds to the strength of the intermolecular interactions (D) in elastic interaction model, the temperature dependence of the HS component changes from a gradual crossover to a first-order transition. Qualitatively, we can rationalize that the gradual two-step SCO observed in **2a′** and **2a″** is related to the elongation and disappearance of the hydrogen bonds NH···Cl^- or three long NH···Br^- bonds, where the volume reduction or expansion of the SCO species due to the spin transition is not effectively transmitted over the crystal lattice. It is also difficult to see the distinct structural parameter causing the gradual SCO in the present series of complexes.

As described above, our attempt to correlate the experimental results to theoretical model calculation is not enough and was not so successful, although the present series of 2D complexes seems to be the most suitable group of model compounds to examine such a correlation. At the least, our present results support the elastic origin of the cooperative nature of SCO: "As the size of each molecule changes depending on its spin state, the elastic interaction among the lattice distortions provides the cooperative interaction of the spin states."[8]

Crystal Structures and Magnetic Properties of [Fe($H_2L^{2\text{-Me}}$)$_2$](BPh$_4$)$_2$·CH$_3$CN (3) and [Fe($H_2L^{2\text{-Me}}$)$_2$](ClO$_4$)$_2$ (4). The crystal structures of **3** and **4** were determined by single-crystal X-ray diffraction analysis at 296 K. Their crystallographic data are summarized in Table 10. The relevant bond distances and hydrogen-bond distances are summarized in Table 11. The coordination angles are given in Supporting Information S4. Compound **3** crystallizes into a monoclinic space group $P2_1/c$ (no. 14). The structure consists of one $[Fe(H_2L^{2\text{-Me}})_2]^{2+}$, two BPh_4^- ions, and an acetonitrile molecule as the crystal solvent. As shown in Figure 24a, the iron(II) ion assumes an octahedral coordination environment with N_6 donor atoms of two tridentate ligands. The Fe−N bond distances are in the range of 2.123(3)−2.201(4) Å at 296 K, consistent with those of the HS Fe^{II} complexes with N_6 donor atoms. One of four imidazole groups per complex molecule (2-methyl-4-formylimidazole residue) is hydrogen-bonded to a nitrogen atom of acetonitrile with a distance of N(6)(imidazole)···N(11)(acetonitrile) = 2.885(10) Å, and the remaining three imidazole groups showed no distinct interaction with the adjacent molecules, though several contacts between NH (imidazole group) and π (phenyl group of tetraphenylborate anion) might be considered as an NH−π interaction. Thus, the complex can be best described as an isolated molecule.

Compound **4** crystallizes into a chiral space group $P3_1$ (No. 144), so that the crystal structure consists of one of two enantiomorphs $[Fe(H_2L^{2\text{-Me}})_2]^{2+}$ and two ClO_4^- anions as the unique unit, and **4** is a conglomerate. The iron(II) ion assumes an octahedral coordination environment with N_6 donor atoms of two tridentate ligands.

Table 10. Crystallographic Data for **3** and **4** at 296 K

complex	**3**	**4**
formula	$C_{70}H_{69}N_{11}B_2Fe$	$C_{20}H_{26}N_{10}Cl_2O_8Fe$
fw	1141.86	661.24
space group	$P2_1/c$ (No.14)	$P3_1$ (No. 144)
a, Å	20.592(6)	13.724(3)
b, Å	13.835(3)	13.724(3)
c, Å	22.403(8)	12.867(4)
β, deg	103.321(12)	
V, Å^3	6211(3)	2098.8(9)
Z	4	3
T, K	296	296
D_{calcd}, g cm^{-3}	1.221	1.569
R, R_w[a]	0.0495, 0.0888	0.0458, 0.1205
Flack parameter		0.000(10)

[a] $R=\sum\|\|F_o\|-\|F_c\|\|/\sum|F_o|$, $R_w=\{\sum[w(F_c^2-F_c^2)^2]/\sum w(F_o^2)^2\}^{1/2}$.

Table 11. Relevant Coordination Bond Lengths (Å) and Hydrogen Bond Lengths (Å) for **3** and **4** at 296 K[a]

complex	**3**	**4**
Fe(1)−N(2)	2.174(3)	2.214(2)
Fe(1)−N(3)	2.186(4)	2.214(2)
Fe(1)−N(5)	2.123(3)	2.150(2)
Fe(1)−N(7)	2.184(4)	2.189(2)
Fe(1)−N(8)	2.201(4)	2.218(2)
Fe(1)−N(10)	2.180(4)	2.147(2)
	Hydrogen Bond	
N(6)···N(11)	2.885(10)	
N(1)···O(1)*		3.008(3)
N(4)···O(8)		2.984(6)
N(6)···O(1)		2.962(5)
N(9)···O(4)**		2.908(4)

[a] Symmetry operations: (*) $-y+1, x-y, z+1/3$. (**) $-x+y+1, -x+2, z+2/3-1$.

The Fe−N bond distances are in the range of 2.147(2)−2.218(2) Å at 296 K, consistent with those of the HS Fe^{II} complexes with N_6 donor atoms. All four imidazole groups per complex molecule are hydrogen-bonded to the oxygen atoms of ClO_4^- ions with hydrogen bond distances of N(1)···O(1)* = 3.008(3) Å, N(4)···O(8) = 2.984(6) Å, N(6)···O(1) = 2.962(5) Å, and N(9)···O(4)** = 2.908(4) Å, where * and ** represent the symmetry operations noted in Table 11. Perchlorate ions play the role of connector to produce a chiral 3D extended structure, as shown in Figure 24b.

The magnetic susceptibilities were measured in the warming and cooling modes. The plots of $\chi_M T$ versus T (see Supporting Information S5) showed that compounds **3** and **4** are in the HS Fe^{II} state ($S=2$) over the entire temperature range of 5−350 K. Perspectives on the structures and magnetic properties of the present series of complexes, the formation of imidazole−Cl^- or Br^- hydrogen bonds can give SCO properties, but the hydrogen bond of imidazole−ClO_4^- or the non-hydrogen bonding cannot give SCO.

Concluding Remarks

Using a tridentate ligand (2-methylimidazol-4-yl-methylidene)histamine, a new family of SCO iron(II) complexes exhibiting 1D, 2D, and 3D structures constructed by hydrogen bonds, as well as isolated structures, can be generated.

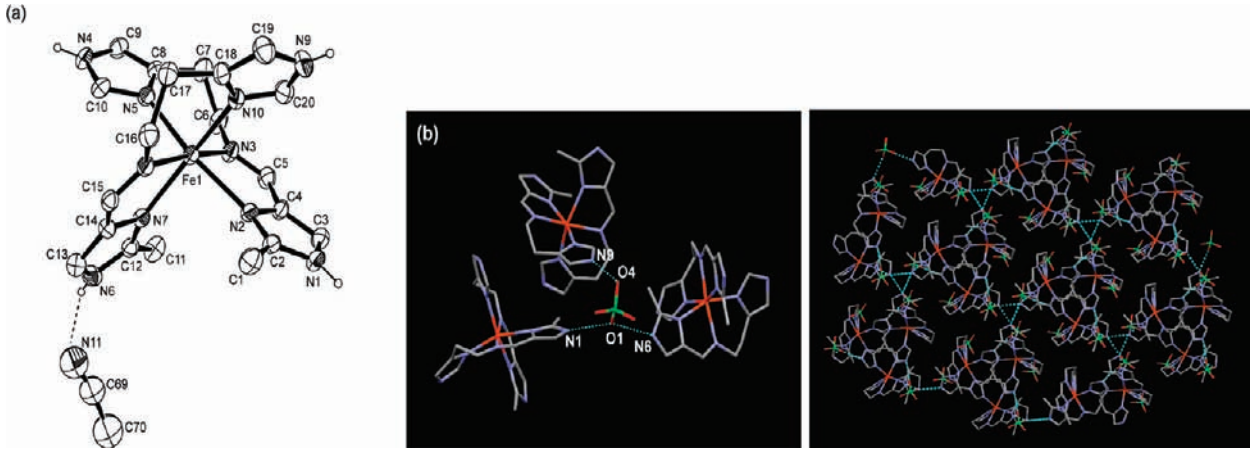

Figure 24. (a) An ORTEP drawing of $[Fe(H_2L^{2\text{-}Me})_2](BPh_4)_2 \cdot CH_3CN$ (**3**), where BPh_4 and hydrogen atoms except for imidazole hydrogen atoms are omitted for clarity. (b) 3D network structure of $[Fe(H_2L^{2\text{-}Me})_2](ClO_4)_2$ (**4**).

The general chemical formulas synthesized in this study are $[Fe(H_2L^{2\text{-}Me})_2]X_2 \cdot$solvent (X = Cl, ClO_4, BPh_4; solvent = 1-PrOH, 2-PrOH, CH_3CN) and $[Fe(H_2L^{2\text{-}Me})_2]X \cdot Y \cdot$solvent (X = Cl or Br; Y = ClO_4, BF_4, PF_6, AsF_6; solvent = EtOH, 1-PrOH). The complex cation $[Fe(H_2L^{2\text{-}Me})_2]^{2+}$ is a chiral species resulting from an octahedral coordination of two unsymmetrical tridentate ligands. Further, the complex cation with four imidazole (NH) sites not only can generate the ligand field strength at the SCO point but also can function to form a hydrogen-bonding network structure. The dichloride complexes $[Fe(H_2L^{2\text{-}Me})_2]Cl_2 \cdot 2\text{-PrOH} \cdot 0.5H_2O$ (**1**) and $[Fe(H_2L^{2\text{-}Me})_2]Cl_2 \cdot 2\text{-PrOH} \cdot H_2O$ (**1′**) have a 1D network structure, where two adjacent chiral complex cations are doubly bridged by two Cl^- ions through NH···Cl^-···HN hydrogen bonds to give a chiral 1D rod. The chiral rods with the same and opposite chiralities are stacked in the crystal lattices to give a conglomerate **1** and a racemic compound **1′**, respectively. Compound **1** showed a two-step SCO, while the desolvated one showed a steep one-step SCO at $T_{1/2}$=180 K. A series of complexes, $[Fe(H_2L^{2\text{-}Me})_2]Cl \cdot X \cdot EtOH$ (X = ClO_4 (**2a**), BF_4 (**2b**), PF_6 (**2c**), and AsF_6 (**2d**)), $[Fe(H_2L^{2\text{-}Me})_2]Cl \cdot ClO_4 \cdot 0.5(1\text{-PrOH}) \cdot 1.5H_2O$ (**2a′**), and $[Fe(H_2L^{2\text{-}Me})_2]Br \cdot ClO_4 \cdot 0.5EtOH$ (**2a″**), have an isomorphous 2D network structure constructed by the NH···Cl^- (or Br^-) hydrogen bonds between the imidazole NH groups of $[Fe(H_2L^{2\text{-}Me})_2]^{2+}$ and the Cl^- (or Br^-) ion, where the anion X is hydrogen-bonded to the 2D network and occupies the space between the puckered 2D layers. They showed a variety of SCO properties depending on the anion, solvent molecule, and bridging halogen ion. The complexes of ClO_4 (**2a**) and BF_4 (**2b**) with smaller anions showed a two-step SCO with one of the largest δT values reported so far, and the SCO occurs accompanying the change of crystal system and space group. The complexes of PF_6^- (**2c**) and AsF_6^- (**2d**) with larger anions showed a one-step SCO, where the crystal system showed no change. The more detailed X-ray analyses for **2a** or **2b** would give the relevant information to reveal the SCO mechanism. The crystal solvent and halide ion also affected the completeness of the SCO in the lower-temperature region and the steepness of the SCO profile, respectively. The experimental results were correlated to the theoretical results on the basis of an Ising-like model. $[Fe(H_2L^{2\text{-}Me})_2](BPh_4)_2 \cdot CH_3CN$ (**3**) has no network structure, where CH_3CN is hydrogen-bonded to the imidazole groups. $[Fe(H_2L^{2\text{-}Me})_2](ClO_4)_2$ (**4**) assumes a chiral 3D network structure constructed by the hydrogen bonds between the imidazole groups of one enantiomorph $[Fe(H_2L^{2\text{-}Me})_2]^{2+}$ and the bridging ClO_4^- ion. Compounds **3** and **4** in the solid state are in a high-spin iron(II) state. Some of the present complexes are obtained as racemic mixtures. Further study on the correlation between chirality and SCO in the present complexes can give insight into the detailed mechanism of SCO.[16]

Experimental Section

General and Materials. All chemicals and solvents, obtained from Tokyo Kasei Co., Ltd., and Wako Pure Chemical Industries, Ltd., were of reagent grade and were used for the syntheses without further purification. All syntheses except for that of **1′** were carried out in a glovebox (MBrawn Unilab) under an inert N_2 atmosphere. The synthesis of **1′** was carried out in the air.

Caution! *The perchlorate salts of metal complexes with organic ligands are potentially explosive. Only small quantities of the compound should be prepared, and they should be handled with much care!*

Ligand. A tridentate ligand, (2-methylimidazol-4-yl-methylidene)histamine, abbreviated as $H_2L^{2\text{-}Me}$, was prepared by mixing a solution of histamine (111 mg, 1 mmol) in 10 mL of ethanol and a solution of 2-methyl-4-formyl-imidazole (110 mg, 1 mmol) in 10 mL of ethanol at room temperature; the resulting solution was stirred for 30 min and then used for the syntheses of all iron(II) complexes without further purification.

$[Fe(H_2L^{2\text{-}Me})_2]Cl_2 \cdot 2\text{-PrOH} \cdot 0.5H_2O$ (1). A solution of $FeCl_2 \cdot 4H_2O$ (94 mg, 0.5 mmol) in 10 mL of 2-propanol was added to the ligand (1 mmol) in 20 mL of ethanol. The solution was allowed to stand overnight at room temperature, yielding orange crystals. Yield: 98 mg (32%). Elem anal. (%) calcd for $C_{23}H_{35}N_{10}O_{1.5}Cl_2Fe$: C, 45.86; H, 5.86; N, 23.25. Found: C, 45.71; H, 5.96; N, 23.33.

$[Fe(H_2L^{2\text{-}Me})_2]Cl_2 \cdot 2\text{-PrOH} \cdot H_2O$ (1′). A solution of $FeCl_2 \cdot 4H_2O$ (94 mg, 0.5 mmol) in 10 mL of 2-propanol was added to a solution of the ligand (1 mmol), and the mixture was stirred at room temperature in the air. A solution of NaBr (52 mg, 0.5 mmol) in 5 mL of 2-propanol was added to the mixture and

(16) (a) Imai, H.; Inoue, K.; Kikuchi, K.; Yoshida, Y.; Ito, M.; Sunahara, T.; Onaka, S. *Angew. Chem., Int. Ed.* **2004**, *43*, 5618–5621. (b) Rikken, G. L. J. A.; Raupach, E. *Nature* **2000**, *405*, 932. (c) Rikken, G. L. J. A.; Raupach, E. *Nature* **1997**, *390*, 493.

filtered. The solution was allowed to stand overnight at room temperature, yielding orange crystals. Yield: 66 mg (22%). Elem anal. (%) calcd for $C_{23}H_{36}N_{10}O_2Cl_2Fe$: C, 45.19; H, 5.94; N, 22.91. Found: C, 45.33; H, 6.11; N, 22.69.

$[Fe(H_2L^{2\text{-}Me})_2]Cl\cdot ClO_4\cdot 0.5EtOH$ (2a). A solution of $FeCl_2\cdot 4H_2O$ (94 mg, 0.5 mmol) in 10 mL of ethanol was added to a solution of the ligand (1 mmol), and the mixture was stirred at room temperature for 10 min. A solution of $LiClO_4$ (106 mg, 1 mmol) in 5 mL of ethanol was added to the mixture, stirred for 10 min at room temperature, and then filtered. The filtrate was allowed to stand at room temperature for several days, during which time orange crystals precipitated from the reduced volume of the solution. They were collected and stored in a sample vial in the air. Yield: 105 mg (34%). Elem anal. (%) calcd for $[Fe(H_2L^{2\text{-}Me})_2]Cl\cdot ClO_4\cdot 0.5EtOH{=}C_{21}H_{29}N_{10}O_{4.5}Cl_2Fe$: C, 40.66; H, 4.71; N, 22.58. Found: C, 40.52; H, 4.90; N, 22.57. IR (KBr): $\nu_{C=N}$ 1631 cm^{-1}, $\nu_{Cl-O}(ClO_4^-)$ 1077−1107 cm^{-1}.

$[Fe(H_2L^{2\text{-}Me})_2]Cl\cdot BF_4\cdot 0.6EtOH$ (2b). Complex **2b** was prepared similarly to **2a**, using $LiBF_4$ instead of $LiClO_4$. Orange crystals were obtained. Yield: 112 mg (37%). Elem anal. (%) calcd for $C_{21.2}H_{29.6}N_{10}O_{0.6}ClBF_4Fe$: C, 41.59; H, 4.87; N, 22.88. Found: C, 41.40; H, 5.08; N, 22.60. IR (KBr): $\nu_{C=N}$ 1631 cm^{-1}, $\nu_{B-F}(BF_4^-)$ 1083−1112 cm^{-1}.

$[Fe(H_2L^{2\text{-}Me})_2]Cl\cdot PF_6\cdot 0.8EtOH$ (2c). Complex **2c** was prepared similarly to **2a**, using KPF_6, instead of $LiClO_4$. Yield: 93 mg (27%). Elem anal. (%) calcd for $C_{21.6}H_{30.8}N_{10}O_{0.8}ClPF_6Fe$: C, 38.17; H, 4.57; N, 20.61. Found: C, 37.95; H, 4.82; N, 20.35. IR (KBr): $\nu_{C=N}$ 1631 cm^{-1}, $\nu_{P-F}(PF_6^-)$ 848 cm^{-1}.

$[Fe(H_2L^{2\text{-}Me})_2]Cl\cdot AsF_6\cdot 0.9EtOH$ (2d). Complex **2d** was prepared similarly to **2a**, using $NaAsF_6$ instead of $LiClO_4$. Yield: 77 mg (21%). Elem anal. (%) calcd for $C_{21.8}H_{31.4}N_{10}O_{0.9}ClAsF_6Fe$: C, 35.96; H, 4.35; N, 19.24. Found: C, 36.07; H, 4.45; N, 19.01. IR (KBr): $\nu_{C=N}$ 1634 cm^{-1}, $\nu_{As-F}(AsF_6^-)$ 706 cm^{-1}.

$[Fe(H_2L^{2\text{-}Me})_2]Cl\cdot ClO_4\cdot 0.5(1\text{-}PrOH)\cdot 1.5H_2O$ (2a′). Complex **2a′** was prepared similarly to **2a**, using 1-PrOH as the solvent. Orange crystals were obtained. Yield: 108 mg (33%). Elem anal. (%) calcd for $C_{21.5}H_{37}N_{10}O_6Cl_2Fe$: C, 37.94; H, 4.40; N, 21.07. Found: C, 37.85; H, 4.55; N, 21.08.

$[Fe(H_2L^{2\text{-}Me})_2]Br\cdot ClO_4\cdot 0.5EtOH$ (2a″). Complex **2a″** was prepared similarly to **2a**, using $FeBr_2$. Orange crystals were obtained. Yield: 97 mg (29%). Elem anal. (%) calcd for $C_{21}H_{29}N_{10}O_{4.5}BrClFe$: C, 37.94; H, 4.40; N, 21.07. Found: C, 37.85; H, 4.55; N, 21.08.

$[Fe(H_2L^{2\text{-}Me})_2](BPh_4)_2\cdot CH_3CN$ (3). To a solution of $FeCl_2\cdot 4H_2O$ (94 mg, 0.5 mmol) in 10 mL of ethanol was added a solution of the ligand (1 mmol). The mixed solution was stirred for 10 min at room temperature and then filtered. To the filtrate was added a solution of $NaBPh_4$ (342 mg 1 mmol) in ethanol, where crude products immediately precipitated, and they were collected by suction filtration. Crude products were recrystallized from acetonitrile, and well-grown yellow crystals were obtained. Yield: 325 mg (57%). Elem anal. (%) calcd for $C_{70}H_{69}N_{11}B_2Fe$: C, 73.63; H, 6.09; N, 13.49. Found: C, 73.82; H, 6.03; N, 13.49.

$[Fe(H_2L^{2\text{-}Me})_2](ClO_4)_2$ (4). To a solution of $Fe(ClO_4)_2\cdot 6H_2O$ (181 mg, 0.5 mmol) in 10 mL of ethanol was added a solution of the ligand (1 mmol). The mixed solution was stirred for 15 min at room temperature and then filtered. The filtrate was allowed to stand for several days, from which yellow rhombic crystals precipitated. Yield: 69 mg (21%). Elem anal. (%) calcd for $C_{20}H_{26}N_{10}O_8Cl_2Fe$: C, 36.33; H, 3.96; N, 21.18. Found: C, 36.97; H, 4.11; N, 21.57.

Physical Measurements. C, H, and N elemental analyses were performed by Kikue Nishiyama at the Center for Instrumental Analysis of Kumamoto University. Infrared spectra were recorded at room temperature using a Nicolet Avatar 370 DTGS (Thermo Electron Corporation) spectrometer with samples in KBr disks. Thermogravimetric analyses were performed on a TG/DTA6200 (SII Nano Technology Inc.) instrument under an air atmosphere using ca. 2 mg of powdered sample at a heating rate of 5 °C min^{-1}. Magnetic measurements were carried out on powdered samples using an MPMS5 SQUID susceptometer (Quantum Design), operating at a 1 K min^{-1} sweeping rate with an applied magnetic field of 0.5 T, in the 5−350 K temperature range. The apparatus was calibrated with palladium metal. Corrections for diamagnetism were applied using Pascal's constants.[17] Mössbauer spectra were recorded using a Wissel 1200 spectrometer and a proportional counter. $^{57}Co(Rh)$ moving in a constant acceleration mode was used as the radioactive source. Hyperfine parameters were obtained by a least-squares fitting of the Lorentzian peaks. Isomer shifts were reported relative to iron foil at 293 K. The sample temperature was controlled by means of a Heli-tran liquid transfer refrigerator (Air Products and Chemicals, Inc.) to within an accuracy of ±0.5 K.

X-Ray Diffraction Analyses. Single-crystal X-ray diffraction measurements were made on a Rigaku RAXIS RAPID diffractometer with an imaging plate area detector using graphite monochromated Mo Kα radiation ($\lambda = 0.71075$ Å). The temperature of the crystal was maintained at the selected value by means of a Rigaku cooling device within an accuracy of ±2 K. The data were collected to a maximum 2θ value of 55°. The data were corrected for Lorentz, polarization, and absorption effects. The structures were solved by direct methods and expanded using the Fourier technique. The structures were refined on F^2 using the full-matrix least-squares method with anisotropic displacement parameters for all non-hydrogen atoms. Hydrogen atoms were fixed in their calculated positions and refined by using a riding model. For the structures of **2a″** in the intermediate and LS states, unit weights in the least-squares calculation were taken. The atomic scattering factors and anomalous dispersion terms were taken from the standard compilation.[18] All calculations were performed using the Crystal Structure crystallographic software package.[19]

Acknowledgment. This work was supported in part by a Grant-in-Aid for Science Research (no. 16205010) from the Ministry of Education, Science, Sports, and Culture, Japan.

Supporting Information Available: X-ray crystallographic files in CIF format and additional tables and figures. This material is available free of charge via the Internet at http://pubs.acs.org.

(17) Kahn, O. *Molecular Magnetism*; VCH: Weinheim, Germany, 1993.
(18) *International Tables for Crystallography*; Kluwer Academic Publishers: Dordrecht, The Netherlands, 1992; Vol. *C*.
(19) (a) *CrystalStructure 3.7.0*; Rigaku and Rigaku/MSC: The Woodlands, TX, **2005**. (b) *CRYSTALS Issue 10*; Watkin, D. J., Prout, C. K., Carruthers, J. R., Betteridge, P. W., Eds.; Chemical Crystallography Laboratory: Oxford, UK.